ABSTRACT

IMPROVING THE STIMULATION SELECTIVITY IN THE HUMAN COCHLEA BY STRATEGIC SELECTION OF THE CURRENT RETURN ELECTRODE

by
Ozan Cakmak

The hearing quality provided by cochlear implants are poorly predicted by computer simulations. A realistic cochlear anatomy is crucial for the accuracy of predictions. In this study, the standard multipolar stimulation paradigms are revisited and Rattay's Activating Function is evaluated in a finite element model of a realistic cochlear geometry that is based on μ-CT images and a commercial lead. The stimulation thresholds across the cochlear fibers were investigated for monopolar, bipolar, tripolar, and a novel (distant) bipolar electrode configuration using an active compartmental nerve model based on Schwartz-Eikhof-Frijns membrane dynamics. The results suggest that skipping of the stimulation point from the vicinity of the cathodic electrode to distant fibers, especially to the low frequency (apical) region of the basilar membrane that is most critical to hearing, occurs more often with monopolar stimulation than other electrode configurations. Bipolar and tripolar electrodes near the apical region did not provide a large threshold margin either before the stimulation skips over distant fibers. On the other hand, the threshold margin could be improved by proper selection of the electrode for the return current with bipolar stimulation, a technique named here as distant bipolar. The results also demonstrate the significance of having a realistic cochlear geometry in computer models for accurate interpretation for multipolar stimulation paradigms. More selective and focal stimulation may be possible by designing the electrode carrier shape and positioning of the current

return electrodes more strategically. This is needed particularly in the apical turn of the cochlea where the current stimulation methods are the least selective.

IMPROVING THE STIMULATION SELECTIVITY IN THE HUMAN COCHLEA BY STRATEGIC SELECTION OF THE CURRENT RETURN ELECTRODE

by
Ozan Cakmak

A Dissertation
Submitted to the Faculty of
New Jersey Institute of Technology
and Rutgers University Biomedical and Health Sciences – Newark
in Partial Fulfillment of the Requirements for the Degree of
Doctor of Philosophy in Biomedical Engineering

Department of Biomedical Engineering

December 2022

APPROVAL PAGE

IMPROVING THE STIMULATION SELECTIVITY IN THE HUMAN COCHLEA BY STRATEGIC SELECTION OF THE CURRENT RETURN ELECTRODE

Ozan Cakmak

Dr. Mesut Sahin, Dissertation Advisor — Date
Professor of Biomedical Engineering, NJIT

Dr. Xianlian Zhou, Committee Member — Date
Associate Professor of Biomedical Engineering, NJIT

Dr. Saikat Pal, Committee Member — Date
Assistant Professor of Biomedical Engineering, NJIT

Dr. Catherine E. Myers, Committee Member — Date
Professor of Pharmacology, Physiology & Neuroscience,
Rutgers-New Jersey Medical School, Newark

Dr. Ozlem Gunal, Committee Member — Date
Assistant Professor of Psychiatry,
Rutgers-New Jersey Medical School, Newark

BIOGRAPHICAL SKETCH

Author: Ozan Cakmak

Degree: Doctor of Philosophy

Date: December 2022

Undergraduate and Graduate Education:

- Doctor of Philosophy in Biomedical Engineering,
  New Jersey Institute of Technology, Newark, NJ, 2022

- Master of Science in Computer Science,
  Southern Illinois University, Carbondale, IL, 2015

- Master of Science in Electrical and Electronics Engineering,
  Mustafa Kemal University, Hatay, Turkey, 2013

- Bachelor of Science in Software Engineering,
  Izmir University of Economics, Izmir, Turkey, 2008

Major: Biomedical Engineering

Conference Papers

Cakmak, O., Pal, S., Ihlefeld, A., Sahin, M., (2019). Finite Element Model of Human Cochlea for Functional Assessment of Cochlear Implant Lead Designs. The Biomedical Engineering Society (BMES) 2019 Annual Meeting

Presentations and Publications:

Cakmak, O., Kazemzadeh, A., Can, D., Yildirim, S., & Narayanan, S. (2012). Root-word analysis of Turkish emotional language. In Proceedings of 4th International Workshop on Corpora for Research on Emotion Sentiment and Social Signals (LREC), May 2012.

Cakmak, O., Kazemzadeh, A., Yildirim, S., & Narayanan, S. (2012, December). Using interval type-2 fuzzy logic to analyze Turkish emotion words. In Proceedings of the 2012 Asia Pacific Signal and Information Processing association Annual Summit and Conference (pp. 1-4). IEEE.

Tonyali, S., Cakmak, O., Akkaya, K., Mahmoud, M. M., & Guvenc, I. (2015). Secure data obfuscation scheme to enable privacy-preserving state estimation in smart grid AMI networks. IEEE Internet of Things Journal, 3(5), 709-719.

My dream throughout my life has

been to be a role model among the disabled. I want to encourage all the

disabled through this quote by one of the most famous people with

hearing loss in history, Thomas Alva Edison:

"Our greatest weakness lies in giving up. The most certain way to

succeed is always to try just one more time."

ACKNOWLEDGMENT

It is a pleasure to thank the many people who made this dissertation possible. First of all, it was a great honor to have had my Ph.D. studies under the direction of Professor Mesut Sahin. I would like to express my gratitude to him for all his invaluable guidance and support while conducting this research.

I also would like to thank Dr. Zhou, Dr. Pal, Dr. Myers and Dr. Gunal for being members of my committee and giving their insightful comments and suggestions through forming my dissertation work.

I'm extremely grateful to Dr. Pal's support and encouragement during my study and would like to thank his Computational Orthopaedics and Rehabilitation Engineering (CORE) Lab members for their support and helpful comments.

I am so grateful to Ferhat Erdogan's help. He has always helped whenever I need help in my dissertation. He is one of the amazing friends that I have met in my life.

I would like to acknowledge the financial support from the NJIT Faculty Seed Grant Award during my Ph.D. studies.

Finally, I would also like to thank my family and friends for their unconditional and loving support over all the time.

TABLE OF CONTENTS

TABLE OF CONTENTS
(Continued)

LIST OF TABLES

LIST OF FIGURES

LIST OF FIGURES

(Continued)

LIST OF FIGURES

(Continued)

LIST OF SYMBOLS

©	Copyright
MP	Monopolar
BP	Bipolar
TP	Tripolar
DB	Distant Bipolar
FEM	Finite Element Method
FDM	Finite Difference Method
σ	Electrical conductivity
AF	Activating Function
ThresMar	Threshold Margin
μ-CT	Micro computed tomography

LIST OF DEFINITIONS

Finite Element Method	A method for numerically solving differential equations arising in engineering and mathematical modeling.
Activating Function	The activation function is a mathematical equation used to estimate the effect of an extracellular field on an axon or neurons.

CHAPTER 1

INTRODUCTION

1.1 Objectives

1.1.1 Aim 1: Constructing a 3D Model of Human Cochlea

Computational models help us gain insight into the underlying mechanisms of cochlear stimulation. They can be used to simulate various types of experiments that are challenging or impractical to perform in animal or cochlear implant patients. Novel electrode arrays can be tested, and the stimulation model can be evaluated iteratively without involving animal or human subjects. Imaging of the human cochlea has played a significant role in the neural modeling for cochlear implants. The computed tomography (CT) image resolution is significantly low. As a result, the images acquired from patients usually do not have sufficiently detailed information about intracochlear anatomy, and thus their usage is limited for the improvement and development of cochlear implants. Gerber et al. gathered a large collection of human temporal bone images acquired using cone beam computed tomography and micro-CT imaging (Gerber et al., 2017a). Micro-computer tomography (μ-CT) images of cochlea are obtained from human subjects (Gerber et al., 2017a) and this data is pre-processed to construct at three-dimensional (3D) model using Simpleware Software in this dissertation. Then, the finite element model (FEM) was developed on this data in COMSOL Multiphysics 5.4a ® Software. After a 3D geometry model is created, the size of the electrode array is determined from the length of the basilar membrane (23 mm). A commercially available standard electrode array (HiFocus 1J) is simulated and placed into the cochlear model.

1.1.2 Aim 2: Modelling Electrical Stimulation of Auditory Nerve Fibers

Neural modeling will help us gain a quantitative understanding of neuronal response to electrical stimulation. We need to understand the mechanism behind the generation of the auditory fiber recruitment and how stimulus parameters may affect neuronal responses to extracellular stimulation. The extracellular potential profile provides a basis for the neural excitation function and thus it has been used while analyzing and understanding the effects of electrode design and position (J. Frijns, De Snoo, & Schoonhoven, 1995a; J. H. Frijns, Briaire, & Schoonhoven, 2000).

We stimulate electrical current spread inside the cochlea while a current is applied through individual electrode contacts. The current spread for various electrode configurations (monopolar, bipolar, tripolar and distant bipolar- a new method introduced in this project) are compared. The results show the difference that the electrode configuration makes in the distribution of the electric fields and how localized the voltage peaks can be in order to activate ganglion cells selectively.

1.1.3 Aim 3: Investigating the Activation Patterns for Alternative Electrode Configurations

The electric potential field distributions in the cochlea in response to stimulation currents through monopolar, bipolar, tripolar and distant bipolar configurations are simulated. In order to translate the electrical potential distributions calculated with the FEM into neural excitation patterns, the electric potentials at the locations of the spiral ganglion nodes of Ranvier are extracted from the FEM model and they are used as an input to an active neuron model developed for cochlear cells by Frijns et al. (J. Frijns et al., 1995a). This model is used to obtain the threshold stimulus currents for each auditory neuron separately.

First, we adjust the cochlear neurons at the micro scale such that the FEM mesh node locations are coincide with the nodes of Ranvier of the cochlear neurons (J. H. Frijns et al., 2000). After the potential values at the nodes of Ranvier for each cochlear neuron are obtained, the potential distributions and the activating functions (F Rattay, 1999) as a function of distance along the length of the nerve fibers are plotted. Activating function (AF) predicts the node of Ranvier at which an action potential starts. Then, we determine the minimum current value, the threshold, at which a neuron fires. These threshold plots across all the auditory neurons are the final output of the model for neural excitation and give us the minimum stimulus current and the node at which each neuron is activated. The spatial selectivity of neural stimulation are calculated by the widths of the threshold curves obtained from the model (Cosentino, Deeks, & Carlyon, 2015).

1.2 Background Information

Cochlear implant (CI) technology has been developed over many years to assist those with substantial hearing loss. Typically, a microphone captures sound and feeds it to a signal processor. The signal processor separates the sound signal into several frequency bands or channels and transmits the filtered signal to electrodes that activate the auditory nerve fibers in the cochlea. The number of electrodes determines the number of spectral stimulation bands. The current commercial stimulation leads contain only 12–22 electrodes although the average human ear contains 30,000 or more auditory nerve fibers. Due to the small number of electrodes, the absence of spectral resolution can result in poor speech perception (Carlyon & Goehring, 2021; Wilson et al., 1991)

CIs have become a standard method of rehabilitation for children and adults with severe to profound hearing loss. CIs are most effective in conveying voice information, particularly in quiet environments. Current CI candidates might anticipate being able to understand speech over the telephone after having an implant. Despite the overall success of CI technology, there is a subset of CI users for whom speech recognition is inadequate (Dhanasingh & Jolly, 2017; Zeng, 2017). Perception of increasingly sophisticated signals, like tonal language comprehension and music perception in the presence of background noise, requires a higher number of stimulation channels to represent the richer frequency content (Carlyon & Goehring, 2021; Lenarz, 2017).

Current focusing and current steering are stimulation techniques aimed to expand the number of unique perceptual channels by adjusting the currents applied through multiple CI electrodes concurrently (Bonham & Litvak, 2008; J. H. Frijns, Dekker, & Briaire, 2011; J. H. Frijns, Kalkman, Vanpoucke, Bongers, & Briaire, 2009; Goldwyn, Bierer, & Bierer, 2010; Kalkman, Briaire, & Frijns, 2015; Koch, Downing, Osberger, & Litvak, 2007; Luo, Wu, & Pulling, 2021; Snel-Bongers, Briaire, van der Veen, Kalkman, & Frijns, 2013). Electrical stimulation through multiple electrodes would normally cause channel interactions, distort the intended perception, and reduce understandability of speech. Experiments have shown, however, that by stimulating two neighboring electrodes simultaneously with a proper ratio of current amplitudes, CI users can sense a pitch between the ones perceived when the electrodes are stimulated individually. Since there is no actual electrode to provide a real stimulation channel at the intermediate pitch, it is referred to as a virtual channel. The virtual channels can be strategically shifted along the basilar membrane by current steering, i.e., adjusting the ratio of currents between the

electrodes. This method can be utilized to increase the number of perceived channels without modifying the number of contacts on the implanted lead (Choi & Hsu, 2009).

Prior to the widespread adoption of the Continuously Interleaved Sampling (CIS) strategy (Wilson et al., 1991), there was significant interest in multipolar stimulation as a means of reducing electrical interactions between the contacts inherent to simultaneous stimulation, which hindered cochlear implant performance at the time (Kalkman, Briaire, & Frijns, 2016). Although the majority of current clinical stimulation strategies do not employ simultaneous activation of cochlear implant electrode contacts, multipolar stimulation has remained an area of research interest, especially as a method of creating more localized regions of neural excitation in order to improve spatial selectivity (J. H. Frijns et al., 2011; Goldwyn et al., 2010; Kalkman, Briaire, Dekker, & Frijns, 2014; Kalkman et al., 2015; Snel-Bongers et al., 2013; Zhu, Tang, Zeng, Guan, & Ye, 2012).

Computational models are ideally suited to elucidate the mechanisms of cochlear stimulation, with novel electrode arrays and stimulation paradigms, that are otherwise impractical or impossible to conduct on patients or in animal models (Hanekom & Hanekom, 2016; Kalkman et al., 2016; Kikidis & Bibas, 2014). Since the development of imaging techniques, it has been apparent that imaging of the human cochlea has provided a powerful tool in audiology and other areas of hearing research (Braun, Böhnke, & Stark, 2012; Cheng et al., 2022; J. H. Frijns, Briaire, & Grote, 2001). However, these cochlear images have not really been utilized to improve the predictions in CI models with few exceptions (Dang, Clerc, Vandersteen, Guevara, & Gnansia, 2015).

In this dissertation, our goal was to evaluate how multipolar stimulation paradigms behave in a realistic human cochlear model for the prediction of neural response. Metrics

were defined to quantify the focality of stimulation for the traditional monopolar, bipolar, and tripolar electrode configurations as well as a novel configuration for current steering that was termed as ‘distant bipolar.’

CHAPTER 2

METHODOLOGY

Overall, the long-term goal of this project is to design electrode geometries that can activate cochlear neurons with higher spatial selectivity and thereby improve the hearing experience of the user by increasing the number of different frequencies that can be perceived. A secondary goal is to reduce the stimulation current and thereby prolong the implanted battery life. The unique aspect of this dissertation is to incorporate a realistic human cochlear anatomy in our simulations and implement various multi-contact electrode configurations tested before using this realistic model, as well as introducing a novel configuration (distant bipolar) that can steer the current in different directions.

This dissertation utilizes finite element modeling as a tool and μCT images of human cochlea for simulations. Chapter 2 describes the methodology of modeling cochlear geometry in two steps. The first step is constructing a 3D model of human cochlea. The second step is modelling electrical stimulation of auditory nerve fibers in Matlab. Chapter 3 covers the third aim where the activation patterns for alternative electrode configurations are investigated. Chapter 4 discusses the simulation results and Chapter 5 is the conclusions.

2.1 Selection of Cochlear Data

In our study, we chose a dataset that included the inner cochlear structures from a published dataset (Gerber et al., 2017a). The dataset, published online by the University of Bern and the Technical University of Munich (TUM), consists of 52 cadaveric human

temporal bone specimens containing the cochlea scanned with clinical cone beam CT (CBCT) at 7.6 μm resolution (Figure 2.1). Twenty-four parts were chosen for manual and semiautomatic segmentations of the cochlea with 5 segments dedicated to the inner structures. The cochlear segments included the perilymph, osseous spiral lamina proper of cochlea, basilar membrane of cochlea, spiral ligament of cochlear duct, modiolus of cochlea, oval window, round window, and the spiral ganglion. The file format is "NII", which stands for NIfTI-1 Data Format (Neuroimaging Informatics Technology Initiative). ITK-SNAP (Yushkevich et al., 2006) software was used to manually alter the segmentations and export the parts as STL (Stereolithography) files that contain the mesh information used to discretize the images. The exported parts are: 1) Cochlea with vestibular canals, 2) Spiral Ligament, 3) Basilar Membrane, 4) Modiolus, 5) Oval Window, 6) Round Window, and 7) Spiral Ganglion (Figure 2.2).

The cochlea is made up of three canals surrounded by a bony structure, the modiolus. These canals are the scala tympani, the scala media and the scala vestibuli (J. Frijns et al., 1995a). The images clearly showed the borders of the scala tympani but did not delineate the scala vestibuli from the scala media due to insufficient image resolution to visualize the Reissner's membrane that separates them, and thus the two compartments were merged into a single segment (Figure 2.2 and Figure 2.3).

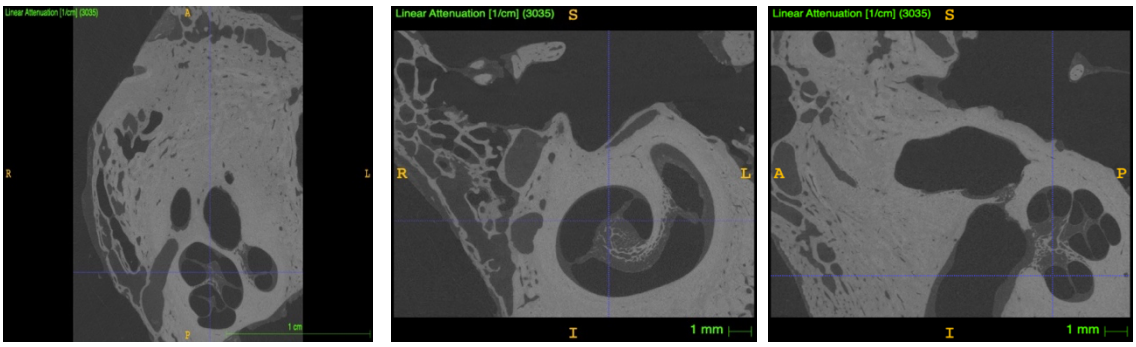

Figure 2.1 A μCT shows (left) axial, (middle) coronal and (right) sagittal planes.

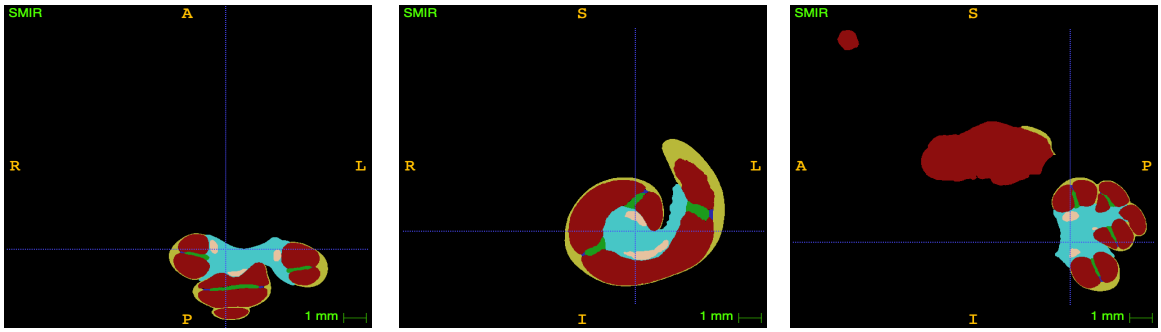

Figure 2.2 The chosen segmentations showing (left) the axial, (middle) coronal and (right) sagittal planes in ITK-SNAP.

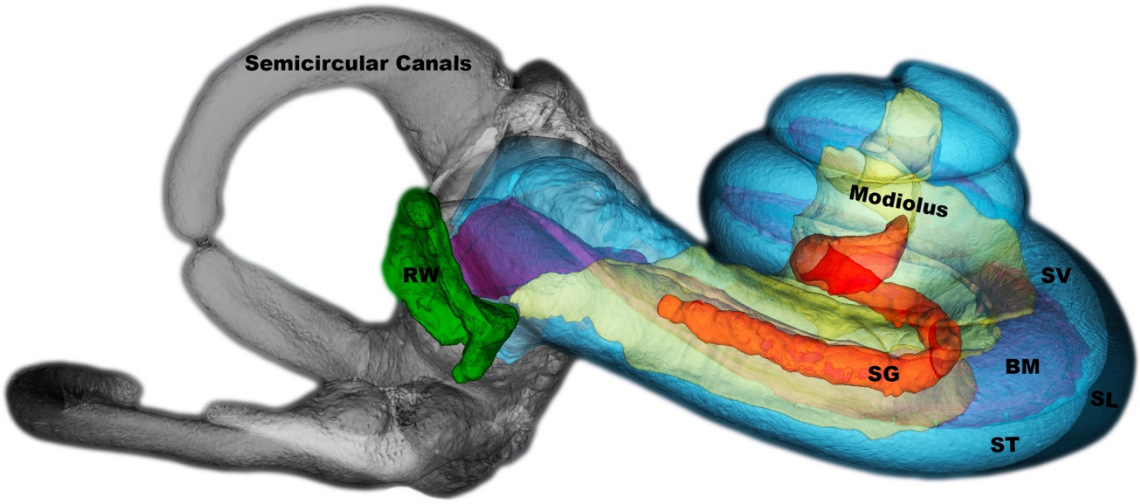

Figure 2.3 The selected dataset is shown as 3D image in ITK-SNAP. The structures are Semicircular Canals, Modiolus, SG: Spiral Ganglion, BM: Basilar Membrane, SV: Scala Vestibuli, ST: Scala Tympani, SL: Spiral Ligament, and RW: Round Window.

2.2 Creating a 3D Cochlea Model

The size of each cochlear image is ~2.20 GB with more than a million voxels. To reduce computation time, we imported the STL files into Simpleware software (Version 2021; Synopsys, Inc., Mountain View, USA) and reduced the size of the mesh for certain computational tasks without sacrificing resolution in desired segments of the model. Then, we exported the parts as STL files. Geomagic software (3D Systems, Morrisville, NC) was utilized to clear the noise, delete unwanted parts, and refine the mesh in the

data. The chosen segmentation data had incomplete vestibular canals. Our aim was to focus only on the cochlea parts. Thus, the vestibular part was removed using Geomagic after we imported STL files from Simpleware. One of the exported parts, the oval window, was also cut open. We removed the spikes, deleted noisy data, and cleaned with smoothing functions. Finally, we remeshed and exported the parts as STL files (Figure 2.4).

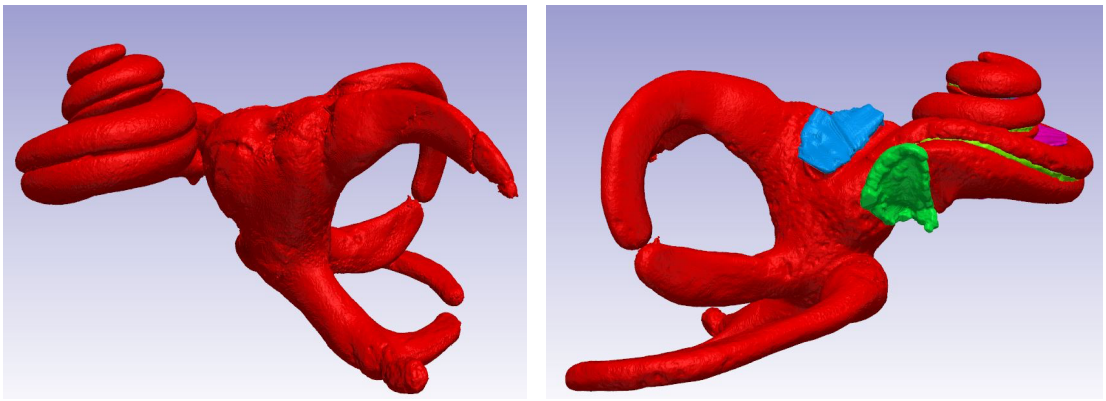

Figure 2.4 Uncompleted vestibular canals (left panel) and b) Oval Window (Blue patch, right panel).

Generating an accurate mesh from 3D CT image data can be challenging, particularly when working with complex geometries such as the human cochlea. HyperMesh software (Altair Engineering, Troy, MI) can create a robust mesh from image data. Triangular elements were used for the mesh. A section of the spiral ganglia was hidden inside the modiolus. This duplicate part was deleted because the spiral ganglia was already imported. Finally, we repaired and smoothened the mesh and then exported as STL files with finer mesh into COMSOL (COMSOL AB, Stockholm, Sweden (Figure 2.5).

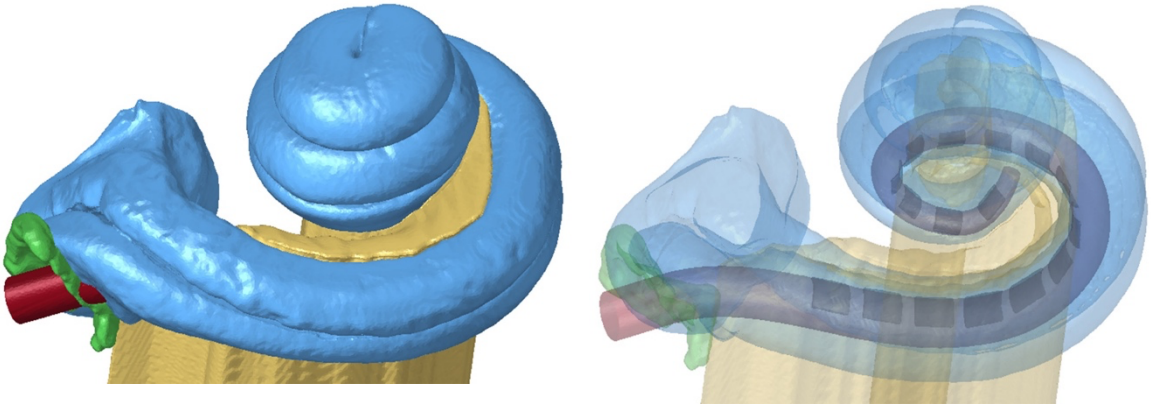

Figure 2.5 Finite element model of the cochlea and electrode array design (in red).

2.2.1 Simulation of a Commercial Electrode

The model was completed by adding the electrode array inside the scala tympani. We used PTC Creo Software (PTC, Boston, MA) for the electrode design that consisted of 16 platinum contacts (conductivity σ=2.5e6 S/m) and a silicon carrier (σ=1e-12 S/m). The electrode array geometry was based on the Advanced Bionics (Sonova, Valencia, CA, USA) HiFocus1J commercial lead and positioned laterally closer to the modiolus inside the scala tympani. The length of the basilar membrane in our human data was ~23mm and the total length of the electrode was ~17mm (Table 2.1 and Figure 2.6).

Figure 2.6 Finite element model of the commercial cochlear electrode array design with 16 contacts (black squares).

Table 2.1 Advanced Bionics Hi Focus 1J Electrode Measures

Electrode Measurements	**Length** (mm)
Electrode array tip diameter (distal)	0.4
Electrode array base diameter (proximal)	0.8
Spacing between active contacts	1.1
Total length of the array	17

Source: Skinner, M. W., Holden, T. A., Whiting, B. R., Voie, A. H., Brunsden, B., Neely, J. G., ... & Finley, C. C. (2007). In vivo estimates of the position of advanced bionics electrode arrays in the human cochlea. Annals of Otology, Rhinology and Laryngology, 116(4_suppl), 2-24.

2.2.2 Meshing All Cochlea Parts and The Electrode

A volumetric mesh was generated with "Extra Fine" element size (Figure 2.7) that consisted of 20,528,625 tetrahedra elements.

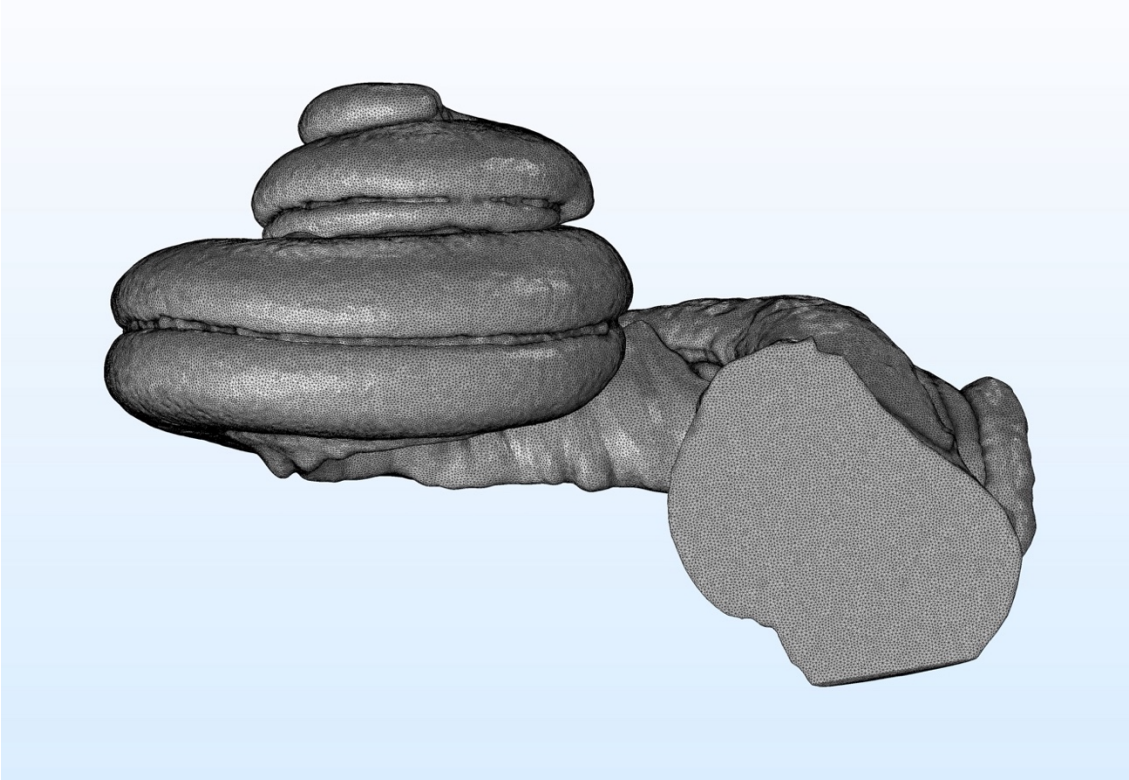

Figure 2.7 The final obtained volumetric mesh of the cochlea.

2.2.3 Electric Potential Distribution Inside the Cochlea

Electric potentials inside the cochlea induced by a current applied to each one of the electrode contacts were simulated by applying the Poisson's equation (Equation 2.1) at each finite element of the model mesh as a volume conductor using COMSOL AC/DC Module.

$$\nabla^2 \varphi = -\frac{I_s}{\sigma} \tag{2.1}$$

where φ is the electrical potential, I_s the current source, and σ the specific conductivity.

Table 2.2 Electrical Conductivity for Various Compartments of the Cochlea

Modeled Structures	**Electrical conductivity (σ)** (S/mm)
Scala Tympani	1.43
Scala Vestibuli	1.43
Basilar Membrane	0.0125
Spiral Ligament	1.67
Modiolus	0.01
Spiral Ganglion	0.33
Electrode Carrier	10^{-15}
Electrode Contact	10^{6}

Source: Frijns, J., De Snoo, S., & Schoonhoven, R. (1995). Potential distributions and neural excitation patterns in a rotationally symmetric model of the electrically stimulated cochlea. Hearing Research, 87(1), 170-186.

Four different electrode contact configurations were tested to investigate the effect on the stimulation selectivity:

1. Monopolar: Cathodic current is applied to one electrode contact and the outer boundaries of the volume conductor were grounded for the return current.

2. Bipolar: Two currents with the same amplitude and opposite polarities are applied to adjacent contacts.

3. Tripolar: Cathodic current is applied to the center contact and anodic currents with the same amplitude to the adjacent two contacts on each side of the cathode.

4. Distant Bipolar: Cathodic current is applied to one contact, and the anodic currents (50% of the cathodic current each) to a distant contact to steer the extracellular field and reduce the spread of the current along the basilar membrane.

A monophasic rectangular current pulse with 0.2 ms duration is used in all electrode configurations, although a biphasic charge-balanced current waveform is typically used in cochlear stimulators. The monophasic waveform was chosen here to eliminate any secondary effects due to the charge balancing phase that may complicate interpretation. The effect of this phase is negligible if there is sufficient time gap between the two phases (Gorman & Mortimer, 1983). The stimulus current pulse was simulated by scaling the extracellular voltage amplitudes generated in COMSOL for a unit current.

2.3 Creating Auditory Nerve Fibers

There are around 30,000 nerve fibers in a healthy human cochlea (Mangado et al., 2018). A human auditory nerve fiber consists of a peripheral axon, the pre-somatic region, the soma, and the central axon. (Figure 2.8)

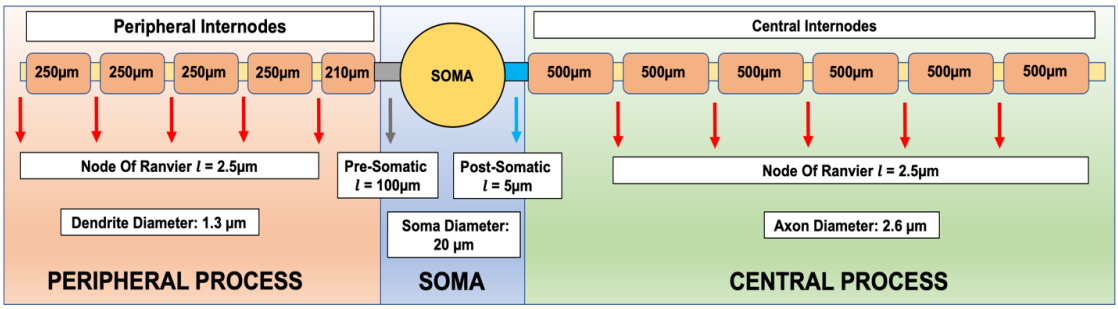

Figure 2.8 Compartmentalized model of an auditory nerve including the peripheral (distal) and proximal fibers, which are myelinated, and the soma. Geometric parameters are adopted from (Potrusil et al., 2020).

Source: Potrusil, T., Heshmat, A., Sajedi, S., Wenger, C., Chacko, L. J., Glueckert, R., . . . Rattay, F. (2020). Finite element analysis and three-dimensional reconstruction of tonotopically aligned human auditory fiber pathways: a computational environment for modeling electrical stimulation by a cochlear implant based on micro-CT. Hearing Research, 393, 108001.

2.3.1 Positioning the Cochlear Neurons in the Extracellular Voltage Field

To predict the electrical behavior of individual auditory nerve fibers, the electrical potentials at all mesh points of the cochlear model were extracted in COMSOL (*scatteredInterpolant* function for linear interpolation) and imported into Matlab (The Mathworks, Inc., Natick, MA, USA). Since the nerve fibers are not visible in the micro-CT images, a priori knowledge of the morphology of the fibers was used to estimate their position and trajectory. We assume that the unmyelinated terminal of the fibers is exactly at the middle point of the basilar membrane between the scala tympani and scala vestibuli (Figure 2.9 - number one). The fiber proceeds into the modiolus and then posteriorly to the spiral ganglion where the cell soma is located adjacent to the scala tympani within the modiolus (Figure 2.9 - number two). The fiber continues radially outward from the modiolus into the internal auditory canal (IAC) where the auditory nerve is formed (Figure 2.9 - number three) by the cumulation of fibers and projects to the auditory cortex. The trajectory of the fiber connecting the unmyelinated terminal to the soma and then to the IAC endpoint that matches the anatomical shape of the cochlea was formed using these three locations marked by three circles in Figure 2.9. Matlab's *csaps* function is used for creating three cubic splines passing through the three coordinates. Then, *cscvn* function is applied for smoothing and interpolating three cubic spline curves (Figure 2.10). Finally, the x, y and z coordinates of all the fibers along 2.5 turns of the cochlea are extracted from *Hypermesh* and then imported into Matlab.

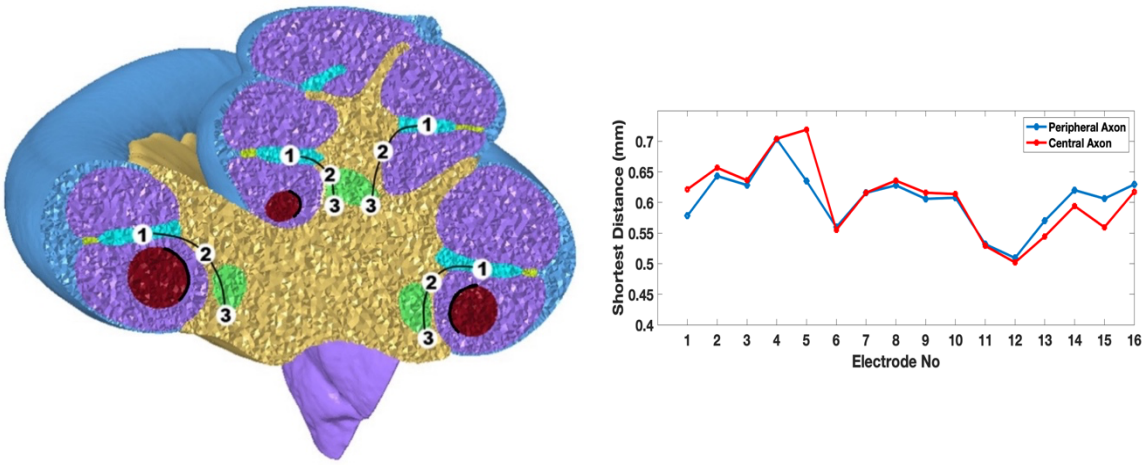

Figure 2.9 Left: A cross-sectional view of the cochlea where the scala tympani (purple), modiolus (yellow), basilar membrane (cyan), spiral ganglion (green) and silicone electrode carrier (red) are shown. The locations marked are: 1. the middle point of the basilar membrane, 2. the cell soma in the spiral ganglion, and 3. a point of passage for the proximal fiber where the cochlear nerve is formed. Right: shortest distances from the center of the electrode contacts to the nearest cochlear fiber. The electrode distance to the closest node of Ranvier in the central and peripheral axons of the nearest cochlear fibers are plotted.

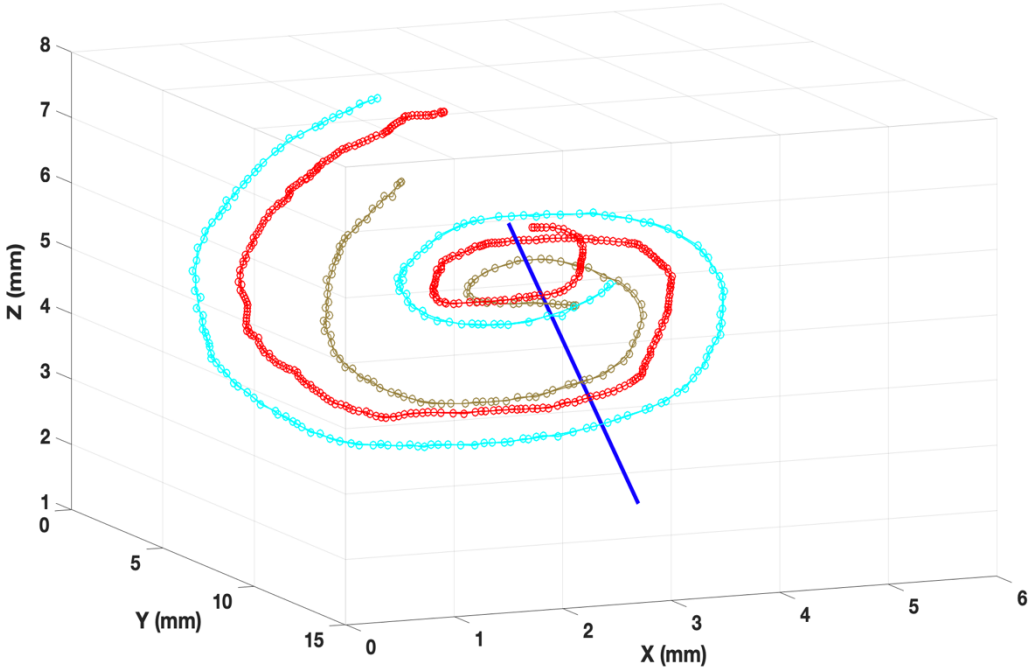

Figure 2.10 Interpolated trajectories using three cubic splines are created through three nerve components marked: 1. the middle point of the basilar membrane (cyan), 2. the cell soma (red), and 3. a point of passage for the proximal fiber in the spiral ganglion (light brown). The blue line shows the central axis of the cochlea.

To connect three splines and then create fiber trajectories, a center reference point is needed. The center point from the top view and the bottom view of the cochlea are marked in *HyperMesh*. These two points are extracted from *HyperMesh* and then imported into Matlab. A line is created connecting these two points to form a central axis for the cochlea (linear line in Figure 2.10). This central line is used as a reference for calculating the radial angles at all points on the three spirals starting from the initial point of the basilar membrane. The points along the three spirals were calculated that are 1° apart as the center line being the apex of the angle. Finally, *csaps* function is used again for creating a cubic spline passing through each set of three points marked on the spirals to form the trajectory of a total of 558 nerve fibers corresponding to one and a half turn of the cochlear spiral (Figure 2.11), similar to a previous study (Kalkman et al., 2014). Also, the positions for the 20 nodes of Ranvier are created on each fiber according to the spacing shown in Figure 2.8. These node of Ranvier coordinates did not fall on the node of the FE mesh (Potrusil et al., 2020). The extracellular voltages at the exact nodal positions were computed by interpolating the voltages at the neighboring nodes of the mesh.

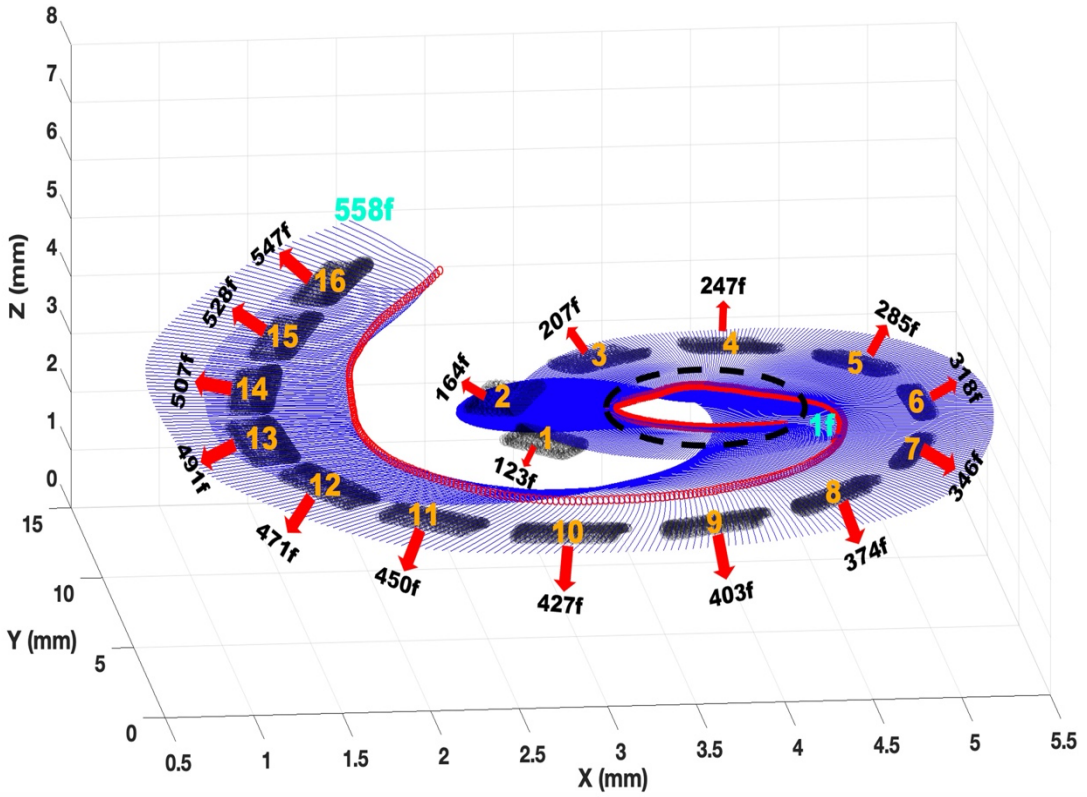

Figure 2.11 Estimated trajectory of 558 auditory nerve fibers (blue) and the somas (red circles), and the electrode contacts (black shading). The fiber numbers nearest to the center of the electrodes are marked down.

2.3.2 Compartmental Active Nerve Model in Matlab

A human auditory nerve fiber consists of a peripheral axon, the pre-somatic region, the soma, and the central axon (Figure 2.8). A compartmental nerve model incorporating the active and passive membrane properties was developed in Matlab, with geometric parameters adopted from (Potrusil et al., 2020), to determine the activation threshold for each one of the auditory nerves. The electric potential field generated varies along the spiral of the cochlea and results in a different response in each nerve fiber. The extracellular electric potentials at the assumed positions of the nodes of Ranvier are transferred from the COMSOL environment to Matlab as an input to the nerve fiber

model in order to predict the threshold current for each fiber and at which node the action potential is initiated (J. Frijns, De Snoo, & Schoonhoven, 1995b; Hanekom, 2001, 2005).

For the active behavior of the nerve membrane in the unmyelinated parts, we used the generalized Schwarz-Eikhof-Frijns (GSEF) auditory nerve fiber model (J. Frijns et al., 1995a). The GSEF model, which is based on Frankenhaeuser-Huxley(FH) (Frankenhaeuser & Huxley, 1964), explains the membrane kinetics of the myelinated nerve fiber in the frog. Frijns *et al*. (J. H. M. Frijns, 1995) modified the FH model for the guinea pig cochlea. They assumed uniform finite-length fibers for all neurons in the cochlea. The equation consists of three time-independent matrices A, B and C (Equation 2.2). A and B are tridiagonal matrices that calculate the resistive coupling between compartments and C is a diagonal matrix containing the nodal capacitances.

$$\frac{dV}{dt} = A\,V + B\,dV_e + C\,[I_{Na} + I_K + I_L] \tag{2.2}$$

V_e represents the extracellular voltages due to the stimulating electrode and V represents the deviation from the resting membrane potential at each node as a function of time to determine if a propagating action potential is generated on the nerve fiber. I_{Na} is the sodium current, I_K is the potassium current, and I_L is the leakage current.

To calculate the nerve fiber responses, extracellular voltages exported from COMSOL were applied as external excitation potentials at the nodes of Ranvier in each nerve fiber. Then, the threshold currents at each node were determined for the occurrence of an action potential by iteratively changing the stimulus current intensity, which is

implemented by scaling the extracellular voltage field generated for a unit current in the FEM. Threshold currents for MP, BP, TP, and DB electrode configurations are computed for all fibers. The nerve fiber is considered to be activated at the current level that stimulates at least one node. The lowest thresholds for all the nerve fibers are plotted to investigate the spatial change of threshold and thus the stimulation selectivity along the cochlear spiral.

CHAPTER 3

RESULTS

3.1 Potential Distributions in the Cochlea

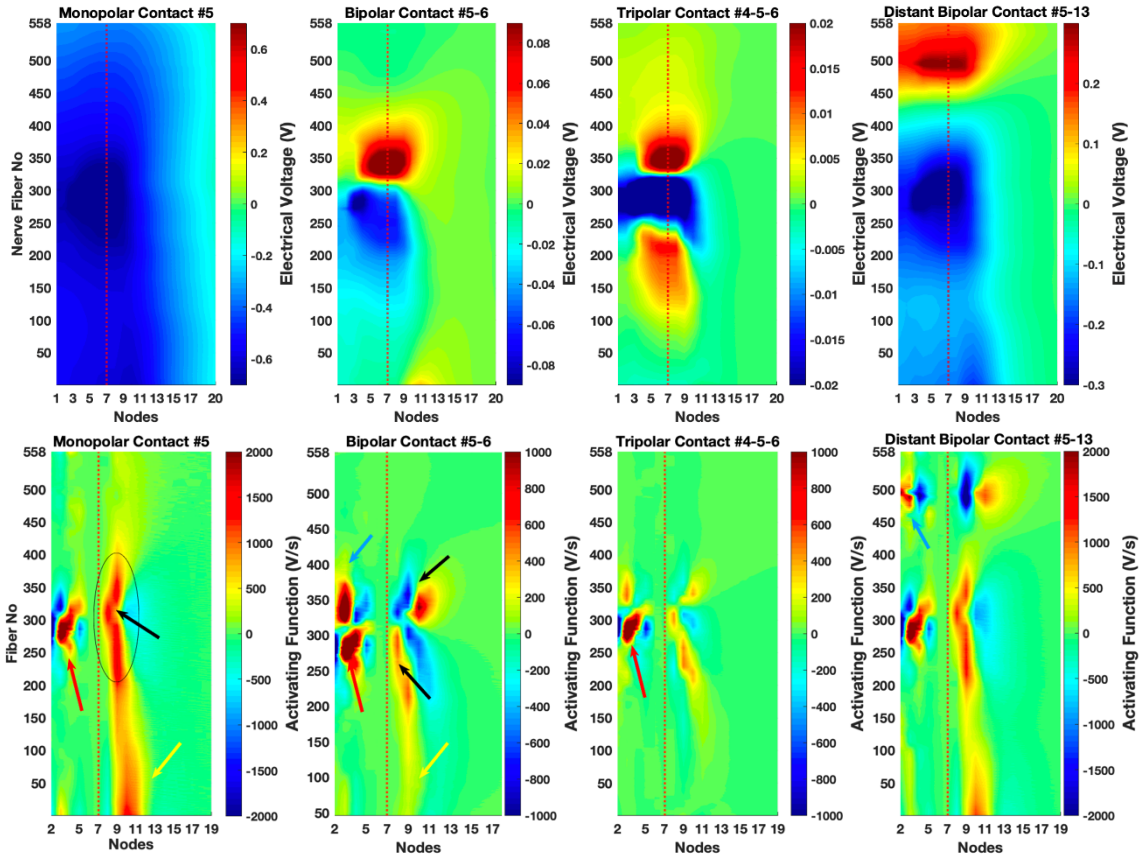

Figure 3.1 Extracellular voltages and activating function as a function of the node and fiber numbers. Top Panel: Extracellular voltage profiles, measured at the nodes of Ranvier, are plotted for all configurations in which contact 5 is the cathode for comparison. Bottom Panel: The activating function calculated according to Equation 3.1 along each fiber. Node 7 corresponds to the soma (red dash lines).

The voltages measured at the nodes of Ranvier of all the cochlear neurons are plotted for four different electrode configurations (MP, BP, TP, and DB) in Figure 3.1 (top panel) where contact 5 served as a cathode in all cases for comparison. Monopolar (MP) field has a wider spread across the fibers than all other configurations and does not switch polarity

along the initial 20 nodes depicted. The peripheral nodes distal to the soma, the soma, and the central nodes close to the soma are exposed to the most negative extracellular voltages inside the basilar membrane.

For the Bipolar (BP), the contact 6 serves as the current return electrode (anode). The BP field has much sharper peaks around the contacts and quickly decreases to zero at the central nodes, but the most negative voltages are about eight times smaller than that of the MP.

For the Tripolar (TP), the contacts 4 and 6, flanking contact 5, serve as the anodic contacts with equal share of the return current. The TP configuration generates even a sharper voltage field by limiting the spread of the current on both sides of the cathodic contact. The negative peak is slightly smaller than the BP peak (-0.07 V vs. -0.09 V). More importantly, in both BP and TP configurations, the spatial extent of the negative field is much shorter than that of the MP across the fibers, i.e., along the basilar membrane.

For the Distant Bipolar (DB), contact 13 (near fibers 485-495) serves as the anode in order to steer the current in a direction orthogonal to the basilar membrane. The DB field represents a midway solution between MP and BP configurations in terms of the voltage spread and the peak amplitudes. The cathodic voltage spreads less and the negative extreme of the voltages are smaller than the MP field (-0.27 V vs. -0.7 V).

3.2 Activating Function

Activating function (AF, Equation 3.1), proposed by Rattay (Frank Rattay, 1986; F Rattay, 1999) and quantifies the rate of increase in the membrane potential at the start of the stimulus pulse, is a reliable predictor of where the action potential is initiated along then

axon, although small deviations may occur in this prediction for long pulse durations (Warman, Grill, & Durand, 1992). The positive values in Figure 3.1 (bottom panel) indicate depolarization of the nodal membrane, and *vice versa*.

$$Activating\ Function\ (AF) = \left[\frac{V_{e,n-1} - V_{e,n}}{\frac{R_{n-1}}{2} + \frac{R_n}{2}} + \frac{V_{e,n+1} - V_{e,n}}{\frac{R_{n+1}}{2} + \frac{R_n}{2}}\right] \Big/ C_{m,n} \tag{3.1}$$

Where n is the node number, R_n is the axoplasmic resistance at node n to the neighboring nodes, and $C_{m,n}$ is the membrane capacitance at node n.

Nearest to Contact 5 are the fibers 260 through 285. There is a positive peak at the third nodes of the fibers between 270 and 300 in the MP plot (red arrow, Figure 3.1, bottom panel). In agreement to this, the lowest stimulation thresholds occur at those fibers according to the simulations of the active axon model in Matlab (Figure 3.3, top panel). The AF plot (MP in Figure 3.1, bottom panel) also suggests that the fibers from 200 to 400 are depolarized at the central nodes of 8 and 9 (black oval). This is mostly due to the anatomical features of the cochlea that nodes 8 and 9 happen to be where the cochlear fiber has a curvature yielding a larger second difference. The threshold and node plots in Figure 3.4 also agree with this prediction. Finally, positive values in the AF predicts low thresholds at node 10 of fibers 1-50 (yellow arrow), as also confirmed by the threshold plot. This low threshold region occurs, however, for a completely different reason. The cochlea spirals inwardly, first moving away from contact 5 and then making a turn and starting to come back towards contact 5 (dash oval in Figure 2.11). Thus, the fibers with the smallest numbers on the inner turn of the cochlear spiral tend to have low thresholds

because of their proximity to contact 5. A similar phenomenon occurs for all the contacts from 3 through 7 (except 5) where some of the fibers within the 1-100 range present even lower threshold than the ones nearest to the cathode due to spiraling of the cochlea.

In the AF plot for the BP stimulation, there is a dark red island between the fibers 270 and 300 in Figure 3.1 (bottom panel), as in the MP plot, for the most distal nodes (red arrow). The second most strong values of the AF function occur for the fibers 325-375, also at the distal nodes, nodes 2-3 (blue arrow) and around the central node 10. This is surprising since the anodic contact (near fibers 300-325) is very close to those fibers. However, the AF peaks on each side of the anodic contact due to the second difference of the voltage along the fibers and gives rise to low threshold regions. There is a low threshold area at the lower end of the fibers (1-50) as in the MP plot (yellow arrow), but the effect is much weaker due to containment of the electric field into a smaller area with the BP configuration. The two red islands in the AF at the central nodes of the fibers within the 200-350 range (black arrows) are not strong enough to impose lower thresholds than those at the proximal nodes of the same fibers. But these peaks tend to widen the threshold plots (see the discussion on the side lobes) because of their wider spread across the fibers.

The AF plot for the TP predicts a focal point at the peripheral nodes of the fibers between 270 and 300 as in MP and BP (red arrow). The fiber curvature effects are small enough that they do not produce other significant local maxima in the activating function. As seen in Figure 3.3, the threshold plot for the shown amplitude range is contained in a much narrower fiber range compared to the other configurations.

Distant Bipolar (DB) activating function is very similar to that of MP around the cathodic contact and at the fibers 1-50, although the secondary peaks are weaker. The

anodic contact (number 13) generates additional low threshold areas at the most distal nodes (node 3) of the fiber numbers around 500 (blue arrow), but fortunately not as strong as those near the cathode.

3.3 Current Threshold vs. Fiber Number

Threshold currents are computed using the compartmental nerve model in Matlab based on the extracellular nodal voltages found from the FE model. Regarding the distant bipolar (DB), the region of neural excitation near the cathode can be shaped gradually by carefully selecting the electrode for the return current, that is by current steering. We took a closer look at how the threshold curve changes when the return current (anode) is applied through different contacts for current steering and compared them with the other three configurations (Figure 3.2). The threshold curve for DB using contacts 5 and 10 resembles the MP curve (black and red respectively) and thus does not provide lower thresholds or better spatial selectivity over MP. As the return current is switched to contacts 5 and 3, the curves (dash lines) start resembling that of BP (green) and TP (blue) in terms of the horizontal spread. However, the minimum threshold currents stay at the low values similar to MP (around fiber 282). This suggests that the placement of the anodic contact can steer the field in a way to reduce the spread of the current along the basilar membrane without increasing the thresholds at the center of the targeted group of fibers.

Minimum currents required to generate an action potential and the node at which it is initiated are plotted for all the fibers in Figure 3.3 for the extracellular nodal voltages shown in Figure 3.1. In general, the action potential initiation point was at nodes 2-3 on the peripheral axon for the fibers with the lowest threshold points. The threshold was higher

for the fibers that are further away from the cathodic electrode and the node of action potential initiation moved more proximally and jumped to the central nodes (nodes > 7). The unexpected finding was that the threshold curves had lobes of local minima on each side of the main lobe, which sometimes had even lower thresholds. These side lobes are a result of stimulations switching from peripheral to the central nodes due to the curved trajectory of the nerve fibers in this voltage field. However, these side lobes are not due to jumping of the stimulus point to opposite side of the spiral as seen with MP having low thresholds at fibers 1-100. These secondary low-threshold regions are an undesired side effects since they will compromise the spatial selectivity of the stimulation.

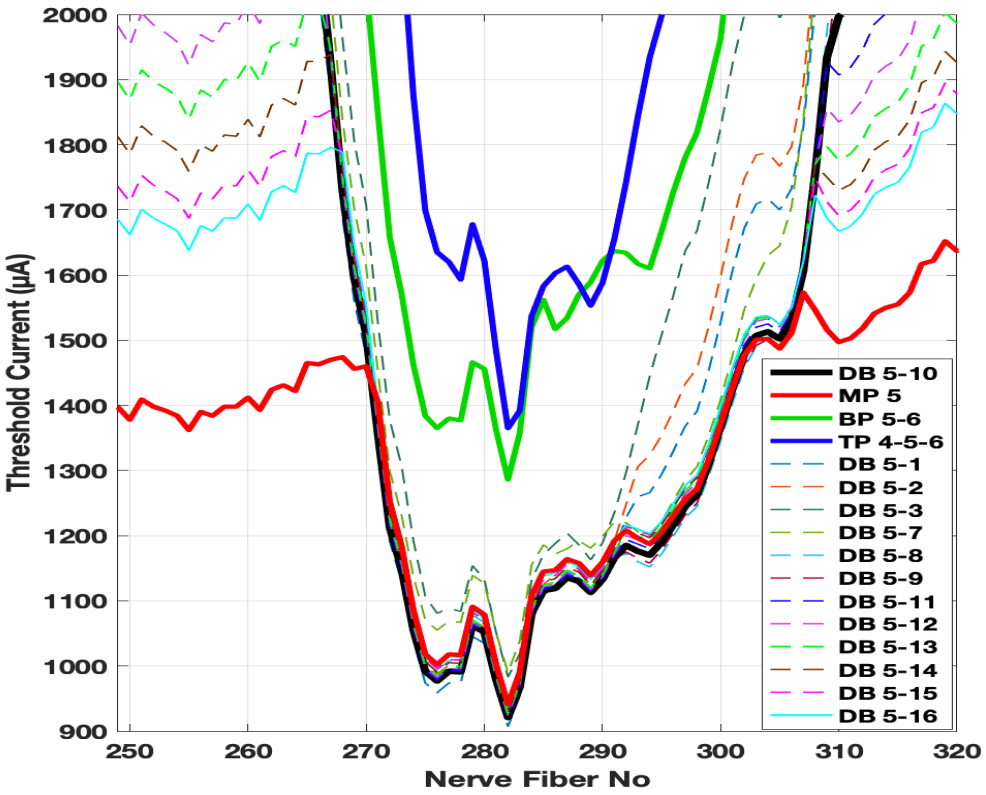

Figure 3.2 Threshold curves for DB stimulation, where the return current (anode) is applied at selected contacts from 1 through 16, is compared with other electrode configurations. A narrow range of fibers are selected on the horizontal axis for better visualization. MP (contact 5): red, TP (contacts 4-5-6): blue, BP (contacts 5 and 6): green, DB (contacts 5 and 10): black, and DB (other contact combinations): dash lines.

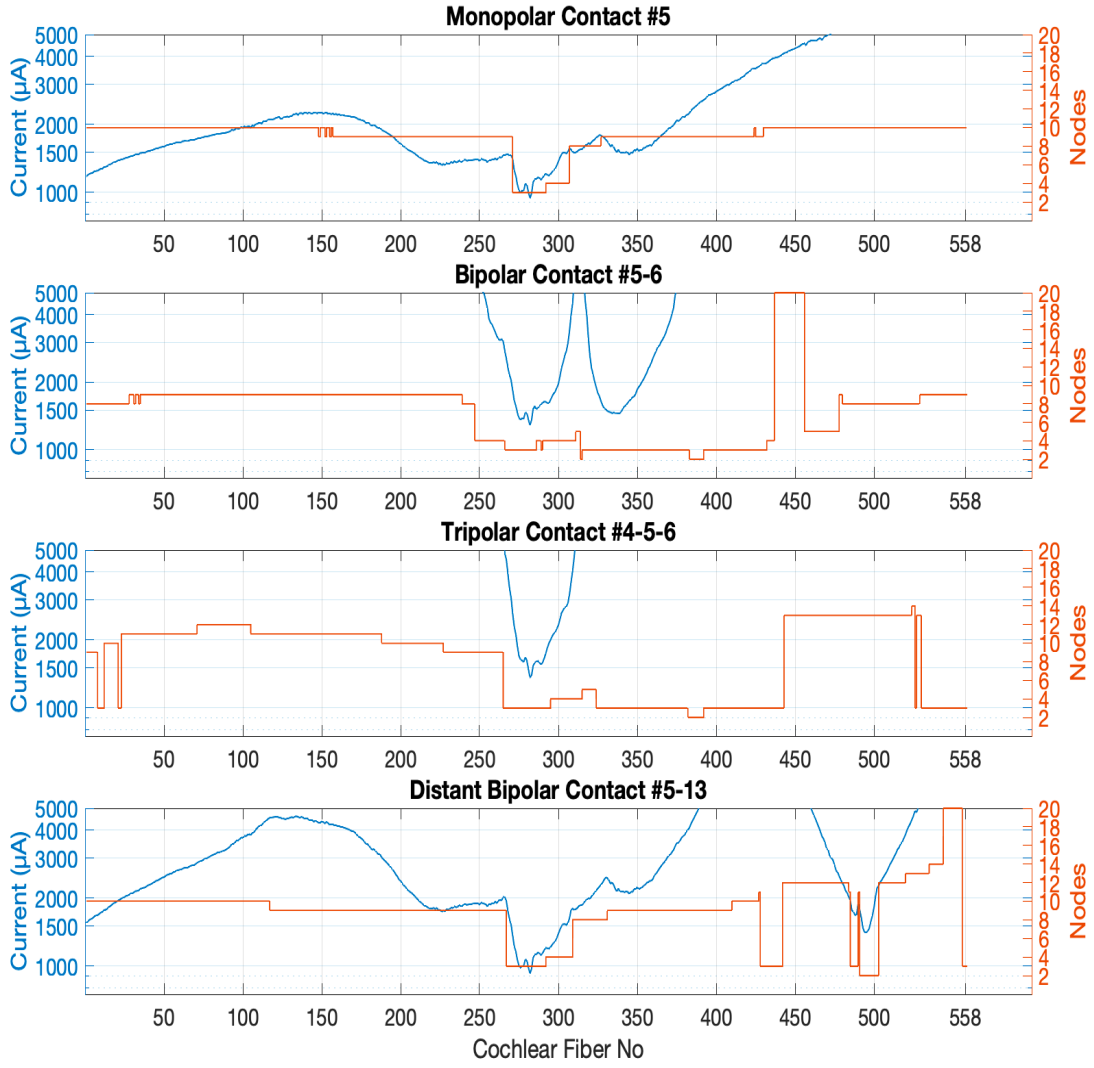

Figure 3.3 Threshold current profiles for all electrode configurations in which contact 5 is the cathode. The red plots indicate the nodes of Ranvier where action potential is initiated in each cochlear neuron. Node 7 represents the soma.

MP and DB configurations have the lowest thresholds (941 μA and 979 μA) on the fibers near contact 5 (node 281) because they produce the largest voltage fields. The BP and TP stimulations have higher thresholds, but narrower spread of excitation across the fibers than the MP stimulation. TP has the highest thresholds (1365 μA at node 281) of all.

The threshold currents and the nodes at which the action potential was initiated are shown for all electrodes in Figure 3.4. For DB, the anodic electrode that produced the largest Threshold Margin (see below for definition) was found for each cathodic electrode individually (Table 3.1). Threshold currents vary depending on the contact number, however, the relative amplitudes for different configurations follow the general trend presented specifically for contact 5 in Figure 3.3. TP and BP have higher thresholds than MP and DB configurations in all cases. In contacts 7-9, the threshold is slightly higher for BP than it is for TP, but they are comparable in most cases. The DB and MP thresholds are also very similar in all cases. Action potential is initiated mostly at the peripheral nodes 3 through 5, but in some cases jumped to the central nodes 8 or 9. This happened in seven electrodes with MP, five electrodes with DB, four electrodes with TP, and three with BP. Stimulation jumped to the central axon with MP and DB in every case where BP and/or TP did the same. Soma is never the lowest threshold point (node 7), possibly due to its high membrane capacitance and small transmembrane resistance.

Table 3.1 Optimum Cathode-Anode Combinations for the DB Stimulation

Distant Bipolar	
Contact 1-4	Contact 9-3
Contact 2-13	Contact 10-3
Contact 3-13	Contact 11-3
Contact 4-13	Contact 12-3
Contact 5-13	Contact 13-3
Contact 6-11	Contact 14-3
Contact 7-4	Contact 15-1
Contact 8-4	Contact 16-1

Finally, we investigated how much would the exclusion of the electrode carrier make in the activation thresholds by removing it from the model while keeping the electrode contacts in place, as also questioned by (Potrusil et al., 2020). As an example, the thresholds for the electrode 5 increased by 36%, 44%, 67%, and 36% for MP, BP, TP, and DB configurations, respectively, in the absence of the electrode carrier, although the overall shape of the threshold plots (as in Figure 3.3) did not change noticeably. Thus, the threshold currents were substantially higher in all cases with no carrier in place and it should be included in the model for accuracy of the predictions.

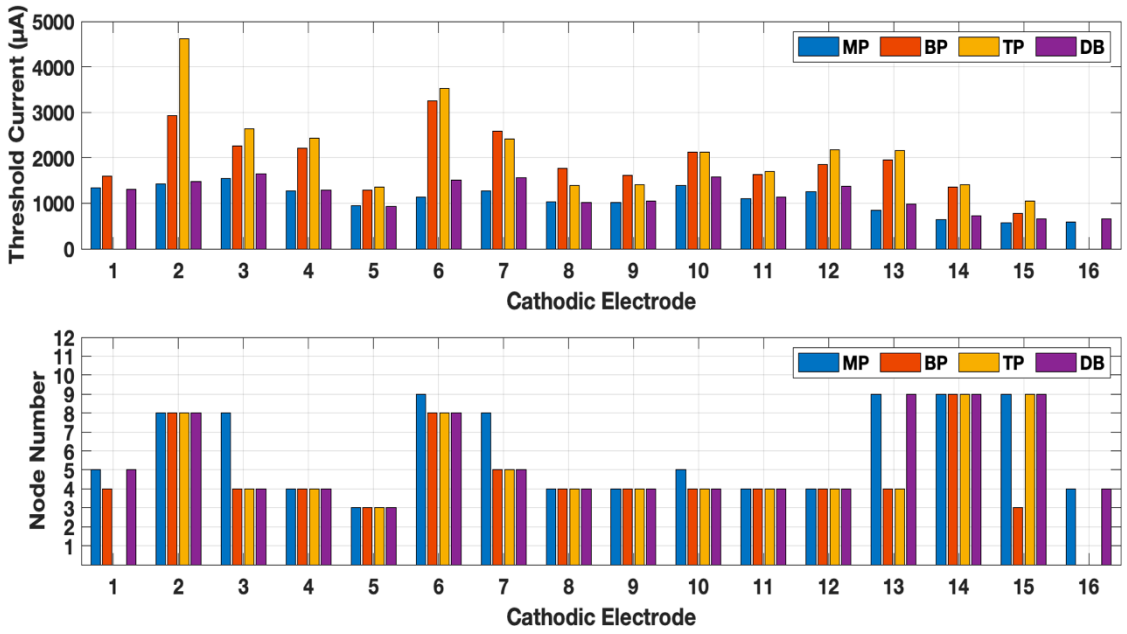

Figure 3.4 Threshold currents (top panel) and the nodes of Ranvier (bottom) at which the action potential is initiated for all electrodes of the array and for monopolar (MP), bipolar (BP), tripolar (TP) and distant bipolar (DB) electrode configurations. Note that x-axis shows the cathodic electrode number in each case. TP configuration is not possible when electrode 1 or 16 is the cathode for the lack of flanking anodic electrodes. BP also does not exist for the 16th electrode for the same reason.

3.4 Threshold Margins

The focality of stimulation determines how many independent channels of stimulation can be achieved with cochlear implants. The spatial extend of the activation before the stimulation point jumps or spills over a distant fiber can be defined as Threshold Margin (*ThresMar*). In our model, there are 16 contacts spanning 558 fibers of the cochlea. Ideally, we would expect each contact to stimulate approximately 35 fibers on average, not more and not less, in order to uniformly cover all the fibers with 16 contacts. We could then define *ThresMar* to quantify how successfully an average of 35 fibers per electrode can be achieved as follows: The threshold current is gradually increased at the cathode until at least 35 consecutive fibers are stimulated near the cathode (Figure 3.5). If a horizontal line (red line) drawn at that current level intersects the threshold curve anywhere else outside the stimulated 35 fibers, those fibers (the second lobe on the right) would be activated by this current as well. The minimum threshold point for this second set of fibers is found and divided by the minimum of the primary set and expressed as a percentage (Equation 3.2).

$$Threshold\ Margin\ (ThresMar) = \left(\frac{Minimum\ Threshold_{\ central\ fiber}}{Minumum\ Threshold_{elsewhere}} - 1\right) \times\ 100 \tag{3.2}$$

This metric quantifies how much the current can be increased before the activation jumps outside the targeted zone of fibers while the total number of fibers in the targeted zone does not exceed a maximum number of 35 for each electrode. For instance, 100% implies that the current can be doubled without off target activation and without stimulation of more than 35 fibers in the targeted zone. A 0% percent or a negative value indicates that

the stimulation jumps to another part of the basilar membrane before even a single fiber is activated in the targeted zone. In Figure 3.5, if the red line did not cross the threshold plot anywhere else, the threshold value at the edge of the 35 consecutive fiber block would be taken and divided by the minimum to find *ThresMar*.

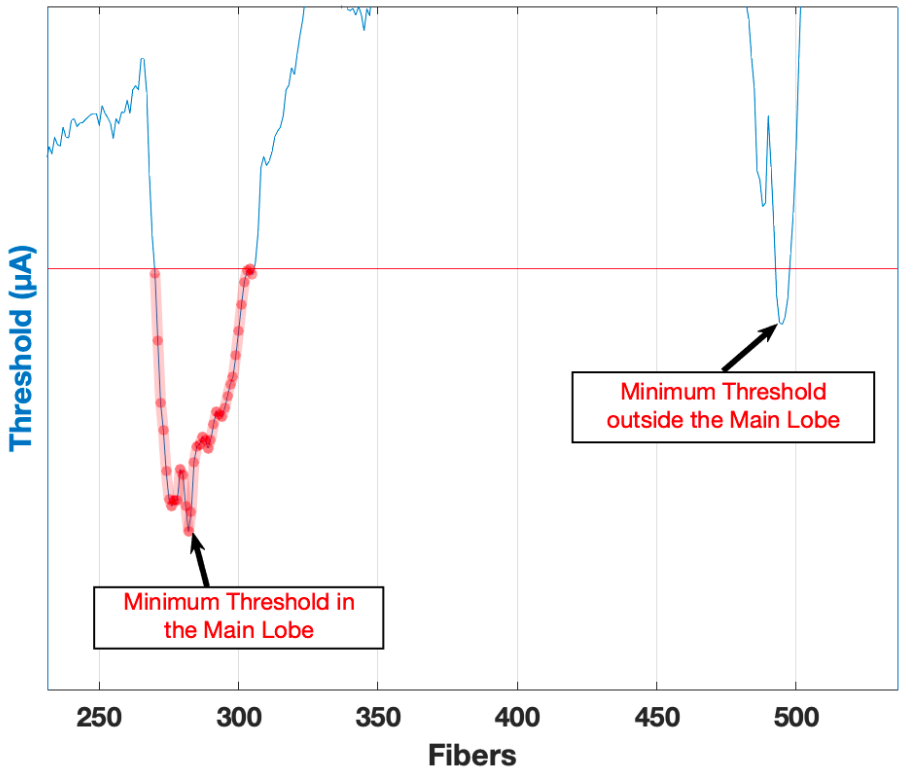

Figure 3.5 The method of calculating the Threshold Margin for an electrode based on the current threshold curve. Example is for TP contacts 7-8-9.

*ThresMar*s (Figure 3.6) show that TP presents the largest percent margins especially in the outer electrodes (>7), followed by MP and DB. BP has the smallest margins in general except in electrode 15. The *ThresMar*s are very low or even negative for most of the configurations with electrodes (cathodic) 1 through 7 where the side lobes tend have a smaller threshold than the main lobe near the cathodic electrode, due to activation at the central nodes. The *mean* ± *standard error* for MP, BP, TP, and DB are

44.7±18.1, 7.68±10.9, 98.8±23.6, 50.1±14.7 percent, respectively. On average, DB increased the *ThresMars* slightly over MP, but TP had the highest margins. BP was the lowest.

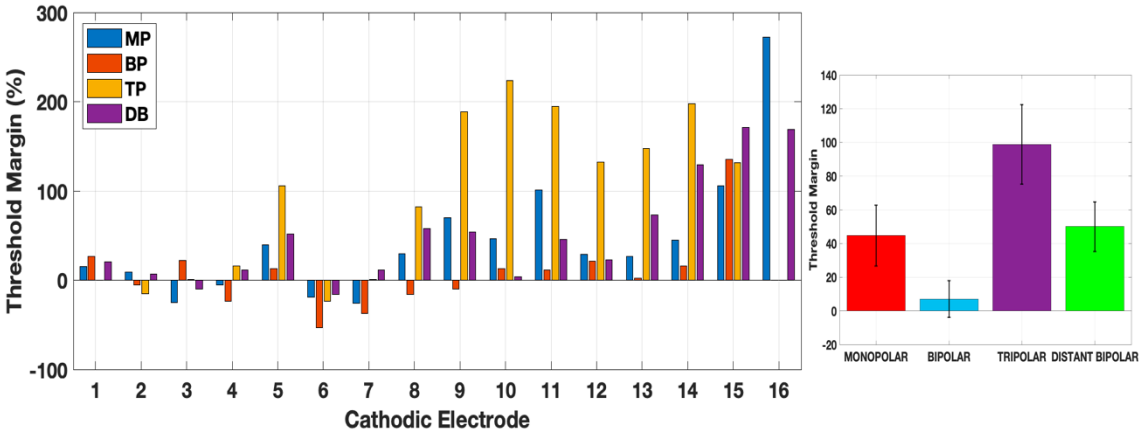

Figure 3.6 Threshold margins for all electrode configurations according to Equation 3.2. The bar plot on the right shows the average and ±standard error for each type.

3.5 Average Number of Fibers per Electrode

An additional piece of information that can be presented here is the actual number of fibers that are stimulated per electrode before the current jumps outside the targeted zone. In a perfect scenario, the number of fibers for all electrodes would be 35. Any value less than 35 at any electrode would imply that some of the 558 fibers will not be accessed when the maximum number of fibers at the other electrodes is limited to 35 in order to keep the stimulation focal.

The maximum number of fibers stimulated without spillover is shown Figure 3.7. The *mean* ± *standard error* for MP, BP, TP, and DB are 23.2±3.6, 10.0±3.4, 19.3±3.6, 20±3 fibers respectively (bar plot in Figure 3.7). A one-way ANOVA confirmed a significant effect of electrode configurations ($F(3,57)=2.846$, $p=0.0455$). Post-hoc

independent-samples t-tests, using a Bonferroni correction (*alpha* adjusted to 0.0125), revealed significant differences between MP and BP only ($t(29)=-2.66$, $p<0.0125$). Electrode 6 is the worst-case scenario where the stimulation jumps to a distant location before even one fiber can be stimulated at the targeted range of fibers for all configurations. This is because electrode 6 is the nearest to the fibers 1-100 (Figure 2.11) and those fibers are activated first before the targeted fibers 300-325.

Although the average across all electrodes do not favor DB over MP or TP, when individual cases were compared, in fact the DB improved *ThresMar*s in 9 electrodes out of 16 and increased the number of fibers stimulated in 5 of those 9. The *ThresMars* was 31%±8.5% (mean±SE, range 6%-84%) higher with DP over that of MP in those 9 electrodes and 3.8±1.8 (mean±SE, range 0 to 15 fibers) more fibers were stimulated per electrodes by those same 9 electrodes.

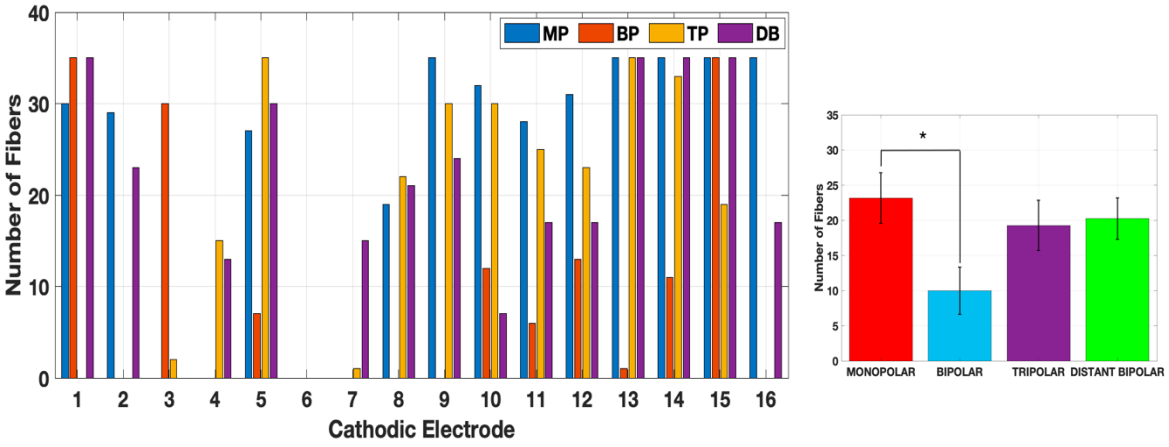

Figure 3.7 Number of fibers stimulated in each electrode configuration before spillover. The bar plot shows the average and ±standard error for each type. Only MP mean is statistically different than BP (ANOVA, alpha adjusted to 0.0125).

CHAPTER 4

DISCUSSION

Our main objective in this study was to revisit the multipolar stimulation methods in a computational model that incorporated a realistic cochlear gross anatomy with complex inner ear geometry that is extracted from human μ-CT images, and that which included a commercial stimulation lead design. We also introduced a novel stimulation paradigm (distant bipolar) for current steering.

4.1 The Activating Function (AF) Patterns

The AF patterns around the cathodic electrodes appeared to be very similar regardless of the electrode configuration (Figure 3.1, bottom row), suggesting minimal interaction from the anodic contacts. Interference between the contacts can increase with larger separations between the basilar membrane and the electrode carrier in the scala tympani (Briaire & Frijns, 2006; J. Frijns, De Snoo, & Ten Kate, 1996; J. H. Frijns et al., 2001; Hanekom, 2001; Seeber & Bruce, 2016). The additional AF peaks that emerged for the anodic electrodes in the BP and DB configurations were much weaker in the case of TP. The interesting, and perhaps unexpected observation was that each electrode had two positive peaks (depolarization) in the AF plots, one at the peripheral and the other at the central nodes, and usually two negative peaks (hyperpolarization) adjacent to the positive peaks. The AF along a straight myelinated axon in a homogeneous medium predicts two hyperpolarized lobes on each side that are four times weaker than the depolarization peak near the cathode in the center (Ranck Jr, 1975; Frank Rattay, 1986, 1987, 1989) This agrees with the AF patterns due to the cathodic contact alone at the peripheral nodes. The

additional depolarized and hyperpolarized points emerging at the central nodes seem to be related to the unique geometry of the cochlear neuron with its curved shape and the presence of the soma in the center. The electrode contacts were almost at equidistance from the peripheral and central axons of the nerve positioned inside scala tympani (Figure 2.9). The relative strengths of depolarizations at the peripheral and central axons would change depending on how the electrode carrier is positioned inside the scala tympani.

The fibers in the ~1-50 range presented low current thresholds with electrodes 5 through 9 of the MP configurations, due to spreading of the voltage field to the apex, and the first activated nodes were the central nodes 10 and 11. This limited the *ThresMar* and lowered the average number of fibers per electrode before the current jumps to the apical fibers. This issue does not appear to be present in the plots of (Kalkman et al., 2015) which could be due to differences in the assumed spatial distributions and the trajectory of the cochlear nerve fibers in the two models. The TP had larger current margins with the electrodes located in the outer spiral of the cochlea. However, BP suffered from stimulation spillover to adjacent fibers due to virtual peaks created in the AF by the anodic contact (Figure 3.1 and Figure 3.3). The DB method introduced in this study searches for an optimum choice for the anodic electrode in order to steer the current and overcome the disadvantages of the MP an BP methods. The DB provided a larger *ThresMar* than MP in most of the electrodes, while having comparable stimulation thresholds (Figure 3.4). Thus, the DB technique can be applied selectively to individual contacts whenever there is potential for improving threshold margins and thereby selectivity.

4.2 Stimulation Threshold Plots

The excitation took place mostly in the peripheral axon, though not always near the end (Frank Rattay, 2008; Frank Rattay, Bassereh, & Fellner, 2017; Rubinstein, 1993) and jumped to the central axons in a few electrodes (Figure 3.4, bottom row). Selectivity with focal stimulation was achieved and was better in the outer turn of the cochlear spiral, with all configurations without resorting to the use of simultaneous pulses for leveraging field interactions. This is in contrast to the findings of (Kalkman et al., 2015) which suggested that selective stimulation is only possible if the excitation occurs in the central axon when the focal electric fields are able to penetrate into the spiral ganglion. The discrepancy in our results may be because we adopted the compartmental neural model developed by (Potrusil et al., 2020) where the peripheral axon is longer, although the neural membrane dynamics were based on the model developed by (J. Frijns et al., 1995b; J. Frijns et al., 1996; J. H. Frijns, Mooij, & Ten Kate, 1994). The relative distance of the electrode contacts to the central and peripheral axons plays a significant role on the focality of the stimulation and the initiation point of the action potential (J. H. Frijns et al., 2009; Goldwyn et al., 2010; Litvak, Spahr, & Emadi, 2007; Seeber & Bruce, 2016; Smit, Hanekom, & Hanekom, 2008). The shortest distance from the electrode centers to the central and peripheral axons of the closest fibers were approximately the same along the entire electrode lead in our model (Figure 2.9), and thus cannot be the reason behind initiation of activation preferably in the peripheral axon. The endings of the fibers had an unmyelinated terminal for 10 μm as in (Potrusil et al., 2020), and those near the cathode were hyperpolarized as seen in the AF plots in Figure 3.1.

Almost all plots of the threshold current as a function of the fiber number contained lobes on each side of the main lobe near the cathode (Figure 3.3). These side lobes were not due to stimulation point jumping to distant fibers, or because of the electric fields generated by the anodic contacts as suggested by (Kalkman et al., 2016) but because of the central nodes having thresholds slightly above that of the peripheral axons. This is clearly shown in the AF plots in Figure 3.1 where the red regions at the central nodes (8-10) span a much wide fiber range than the ones in the peripheral nodes. This must be because of the fact that the central axons draw closer to each other as they travel down the modiolus. As a result, the electric field of a similar spatial extent affects a large number of central axons in the modiolus than the peripheral axons in the basilar membrane. Phased arrays were suggested as a potential solution to eliminate these side lobes (J. H. Frijns et al., 2011). The DB method proposed here also weakens the side lobes by reducing the AF peaks at the central nodes (Figure 3.1) and increases the *ThresMar*. Note that the improvements in selectivity suggested by the results of the present study can be combined with other methods that can achieve focal stimulation (e.g., simultaneous multi-contact stimulation or using different temporal waveforms) since the electric fields in volume conductors scale linearly and they are additive.

The threshold differences between the peripheral and central axons are smaller for the electrodes in the apex, probably because the central axons are even more closely packed than they are in the outer spiral of the cochlea. As a result, the *ThresMars* are very small or negative for the first seven electrodes regardless of the configuration (Figure 3.6) in agreement with (Bai et al., 2019). In order to achieve selective stimulation and larger current margins in the apex, the electrodes should be made smaller and positioned with

smaller spacing in between and perhaps closer to the basilar membrane inside scala tympani.

4.3 Model Validation

Despite the lack of electrophysiological data to validate our results, the insight that can be gained through modeling is invaluable. The AF closely agreed with the fibers of lowest threshold predicted by the active compartmental model, and it was useful to gain insight for the mechanisms underlying the stimulation profiles with multipolar electrode configurations and a novel method, the distant bipolar method. Our nerve model adopted from (Potrusil et al., 2020) contained 20 nodes including the soma. The simulations were run with lower number of compartments, by removing the 5 most proximal ones, in order to check if the number of compartments were sufficient for the accuracy of threshold predictions. The threshold currents were less than 5% different with the shorter model indicating that adding more compartments would not change the results significantly. We also checked if the boundary conditions would introduce significant changes in the results. We made the surrounding box around the cochlea smaller (50 mm x 50 mm x 50 mm) than the current size (100 mm x 100 mm x 100 mm), which altered the extracellular voltages again less than 5%. The mesh size inside the cochlea was the smallest available in COMSOL and much smaller than the spatial extent of any local variations seen in the voltage fields.

4.4 Isotropic Conductivity

Reported cochlear implant models typically use isotropic conductivities for various compartments of the cochlea. This may be sufficient for most cochlear inner structures. But the electrical currents cannot be conducted equally well in all directions in the

modiolus because the cochlear nerve fibers introduce a great deal of anisotropy and take up a notable size of space. Adding anisotropy to the cochlea model to account for the presence of such structures could have a significant effect on the results and should be implemented in the future for more realistic results (Fellner, Heshmat, Werginz, & Rattay, 2022; Kalkman et al., 2016). A detailed geometry for the human head could also be incorporated into the model to achieve more realistic distributions of the voltage field at the boundaries of the cochlea. Our experience, however, agrees with another report (Potrusil et al., 2020) that the boundary conditions mostly add a common shift to the voltage and do not affect the AF profiles.

4.5 Trajectory of the Cochlear Nerve Fibers

In our model, cochlear nerve fibers had an assumed smooth trajectory from the basilar membrane to the modiolus, a fixed length, and regular spacing, simply because the μ-CT images are not able to capture the trajectory of individual fibers. In the human cochlea, the fibers are bundled after passing the Organ of Corti through the basilar membrane (Cakir, Labadie, & Noble, 2019; Frank Rattay & Tanzer, 2022). The actual trajectories of these fibers can vary considerably along the turns of the cochlea. Low threshold points will occur along these fibers whenever there is bending or an inhomogeneity in the extracellular conductivity at the micro scale, as suggested by (Potrusil et al., 2020). In addition, to other reports (Badenhorst, Hanekom, & Hanekom, 2016) and (J. Frijns, Van Gendt, Kalkman, & Briaire, 2015) found that adding stochasticity to the cochlear models plays a significant role in prediction of the stimulation thresholds. The present study was intended to provide a general understanding of how traditional multipolar stimulation results are affected by a

realistic gross cochlear geometry and introduce the DB method, and therefore does not challenge the findings of other reports incorporating more sophisticated models of the cochlear nerve anatomy and membrane physiology.

4.6 CT vs. μ-CT

In comparison to the size of the human cochlea and its internal structures, the resolution of contemporary clinical CT images is quite poor. As a result, images obtained from patients often lack information on the intracochlear anatomy and are therefore of limited use for the development of artificial hearing implants (Gerber et al., 2017b). To compensate for the low resolution of clinical CT imaging, several attempts have been made to extract the desired geometric information (e.g., total cochlear duct length, position of the basilar membrane) from surrogate measurements made from CT images (Erixon & Rask-Andersen, 2013; Escudé et al., 2006). However, the intricacy of cochlear anatomy reduces the efficacy of these techniques. With the development of current imaging techniques such as micro computed tomography (μ-CT), the ability to gather comprehensive imaging information has enabled researchers to obtain previously inaccessible aspects of the cochlear structures (Teymouri, Hullar, Holden, & Chole, 2011). The reduced size of the scanning field of view and the high radiation dose necessary to attain a high degree of image quality are the current limits of this technology for clinical integration.

CHAPTER 5

CONCLUSION

Overall, the results demonstrate once more that the stimulation patterns in a real human cochlea may not be as uniform as predicted by idealized cochlear geometries used in some reported models (Frank Rattay, Leao, & Felix, 2001). It is likely that each human cochlea will have slightly different anatomy and local inhomogeneities. Therefore, the optimum electrode configuration and the optimum set of current thresholds for each electrode will have to be determined in each subject individually. In the past, the traditional multipolar stimulation paradigms only considered adjacent placement of the electrodes or skipping one or two contacts in the bipolar configuration for current steering (J. Frijns et al., 1995b; J. Frijns et al., 1996; J. H. Frijns et al., 1994; Heshmat, Sajedi, Schrott-Fischer, & Rattay, 2021). The optimum choice for the return current may be a distant electrode, as suggested by our results, in order to achieve larger current margins and thus selectivity. The commercial cochlear leads currently do not allow different electrode configurations most likely because of the limitations on the battery life. Complex electronics and current drivers that consume extra energy are required to implement such variations. Nonetheless, as the longevity of implantable batteries improves with technological advancements in that field and switch-mode electrode driving system that can also improve battery life are incorporated into the cochlear implants, these alternative stimulation paradigms should become available for the cochlear implant users in the near future.

APPENDIX A

EXTRACEULLAR VOLTAGE PROFILES

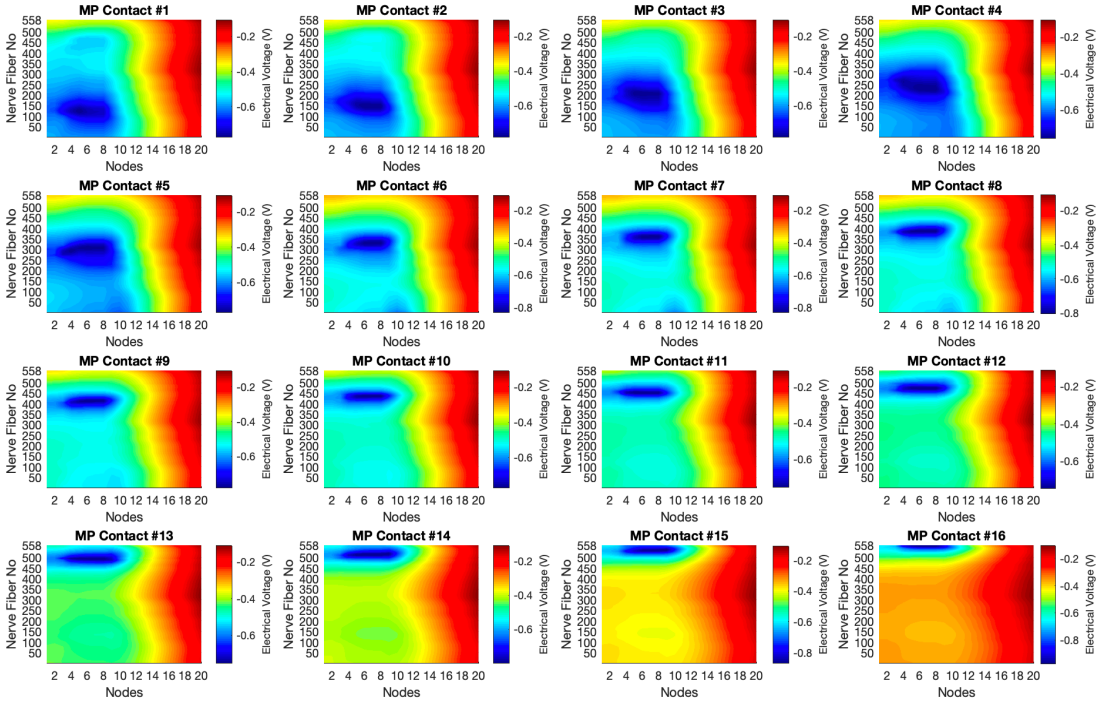

Figure A.1 Extracellular Voltages Profiles for Monopolar Stimulation.

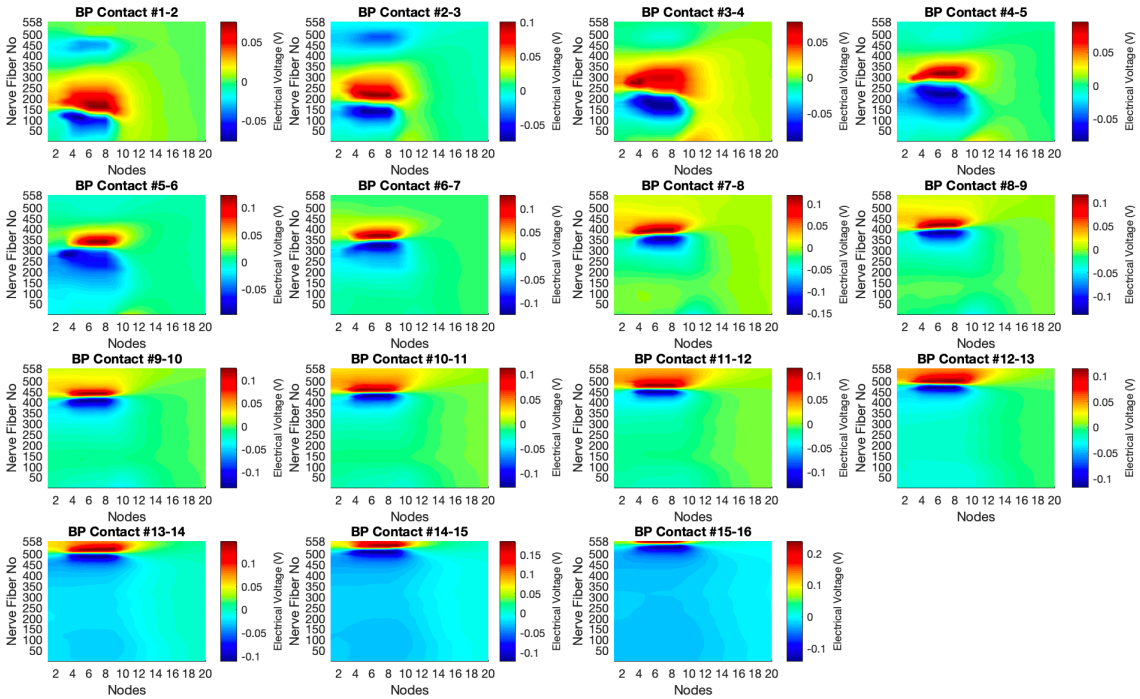

Figure A.2 Extracellular Voltages Profiles for Bipolar Stimulation.

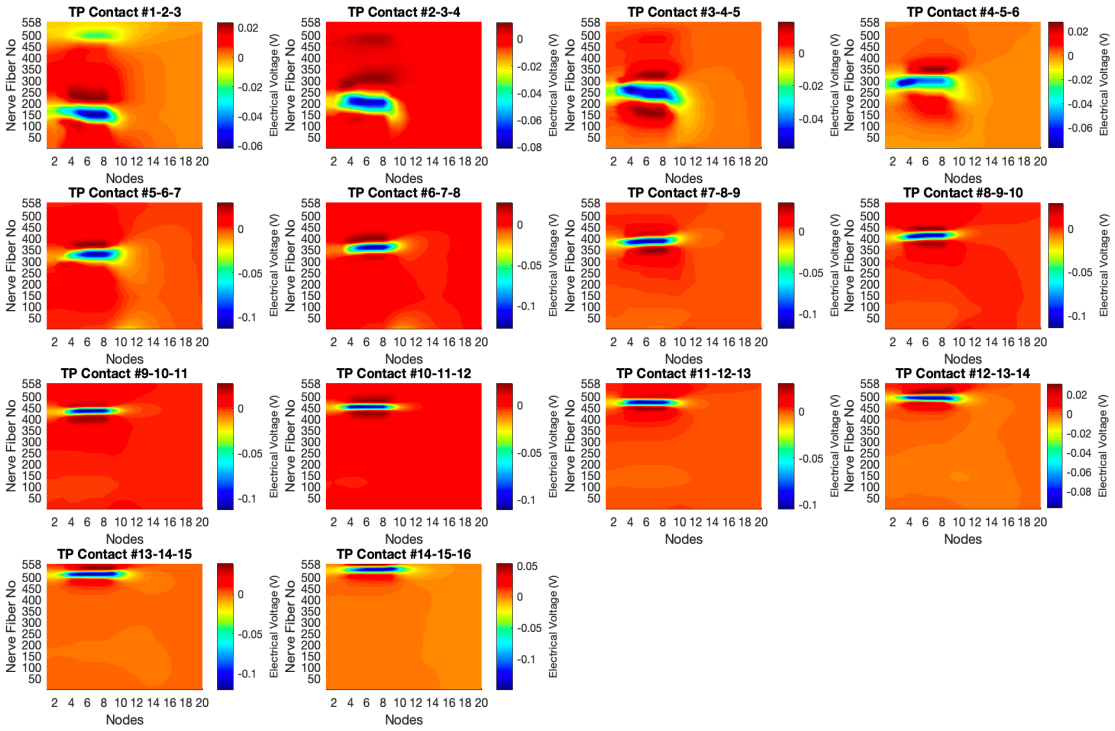

Figure A.3 Extracellular Voltages Profiles for Tripolar Stimulation.

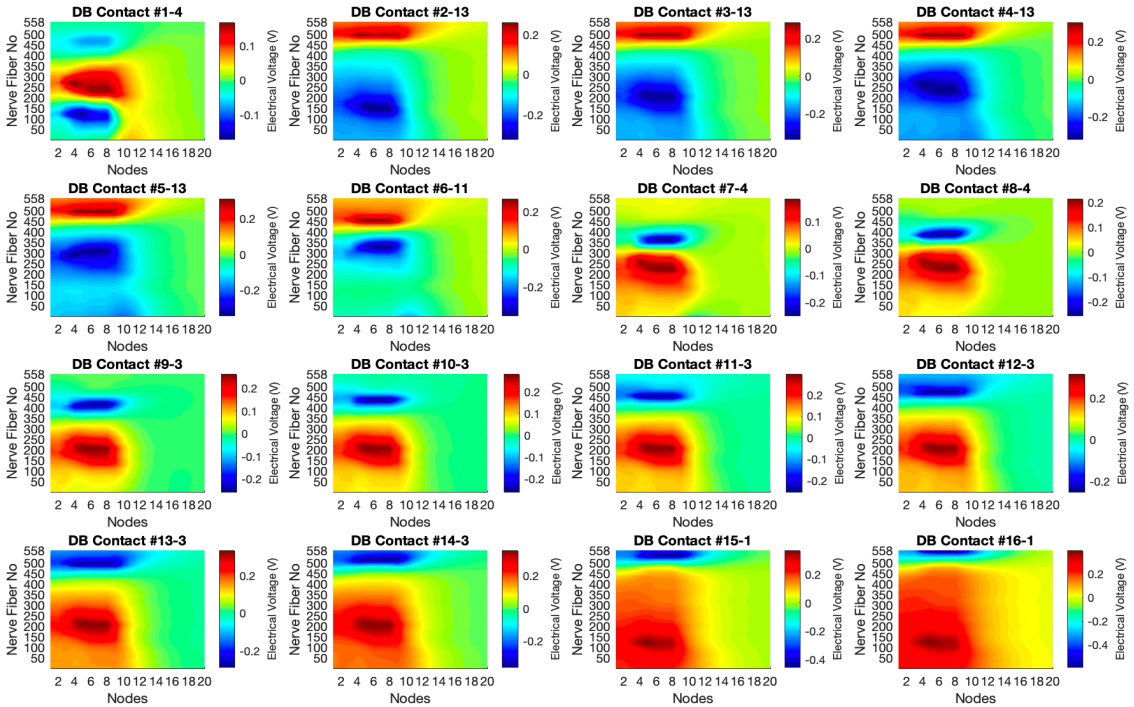

Figure A.4 Extracellular Voltages Profiles for Distant Bipolar Stimulation.

APPENDIX B

ACTIVATING FUNCTION PATTERNS

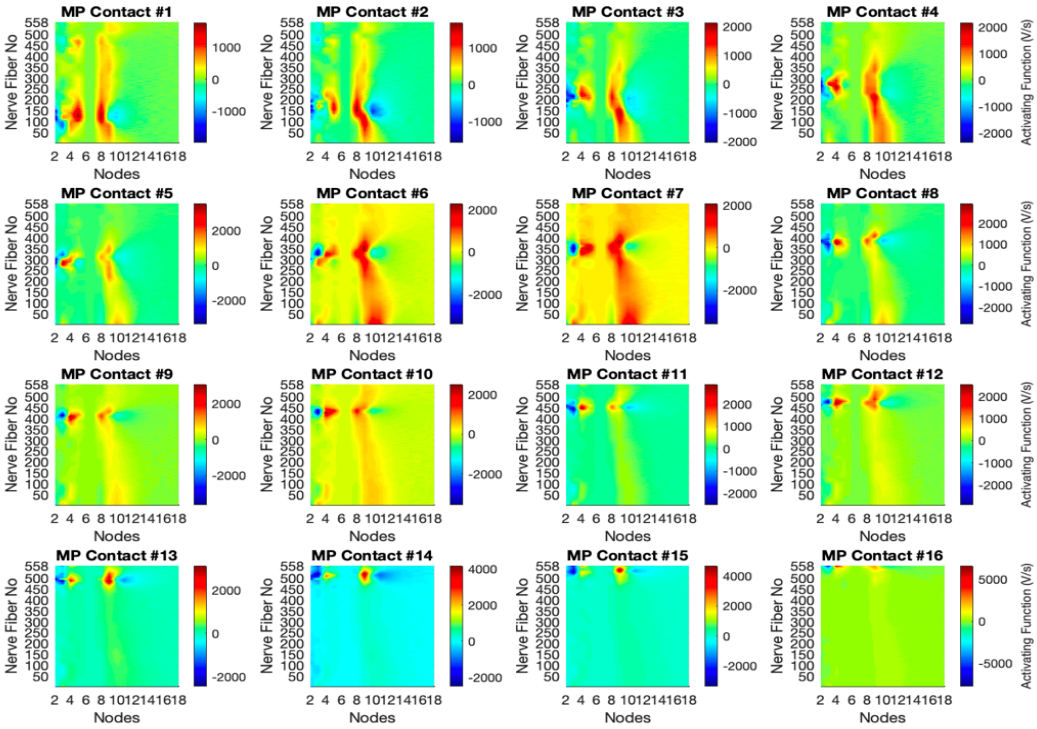

Figure B.1 Activation Function Plot for Monopolar Stimulation.

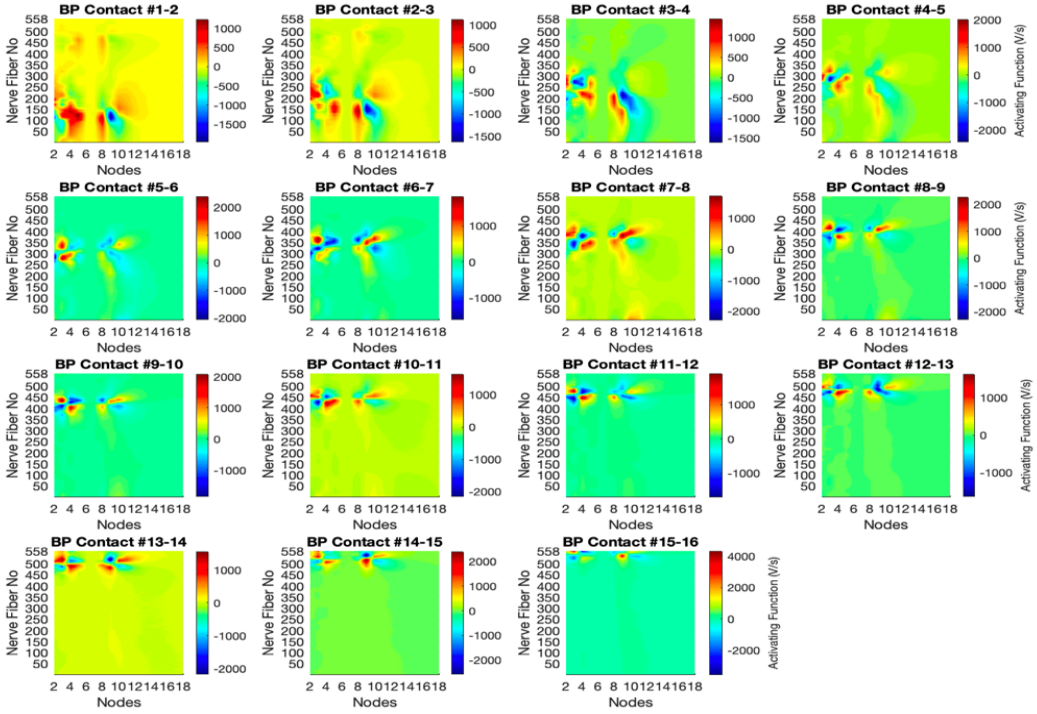

Figure B.2 Activation Function Plot for Bipolar Stimulation.

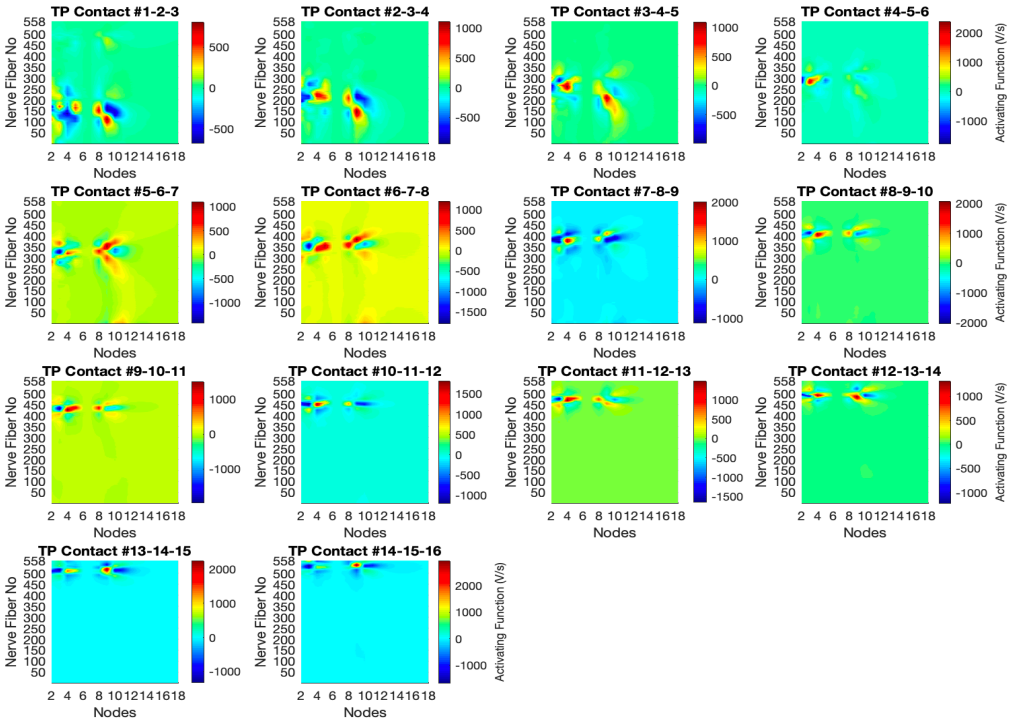

Figure B.3 Activation Function Plot for Tripolar Stimulation.

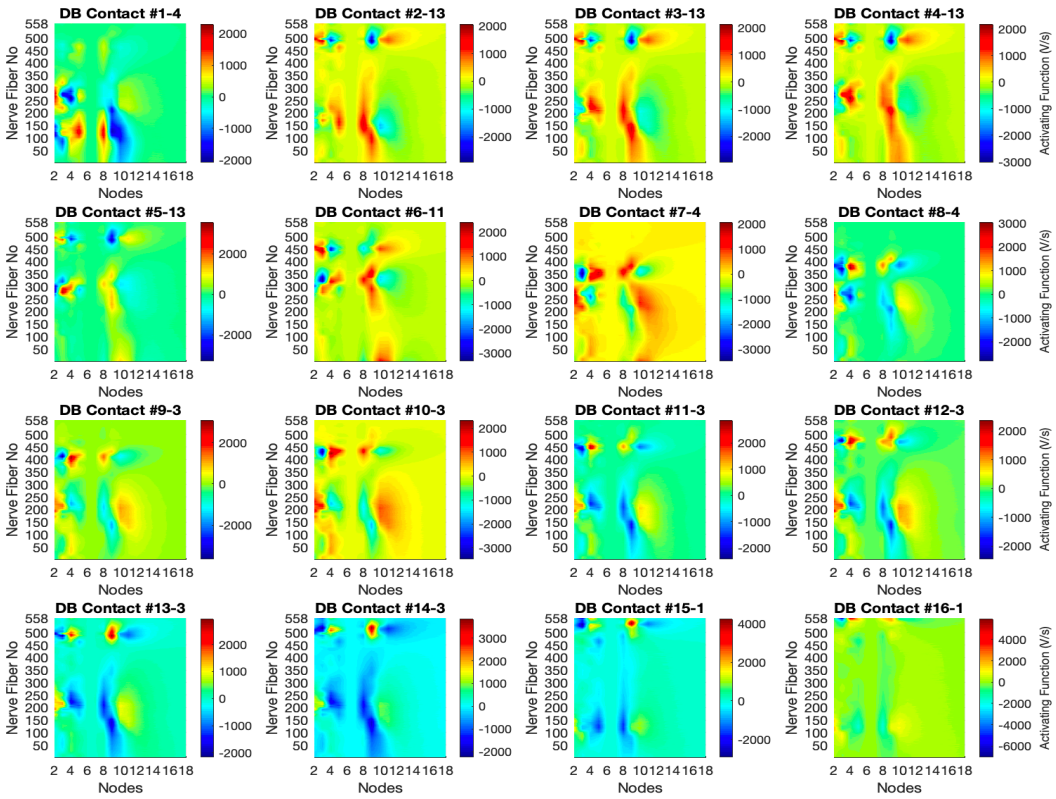

Figure B.4 Activation Function for Distant Bipolar Stimulation.

APPENDIX C

THRESHOLD CURRENT PROFILES

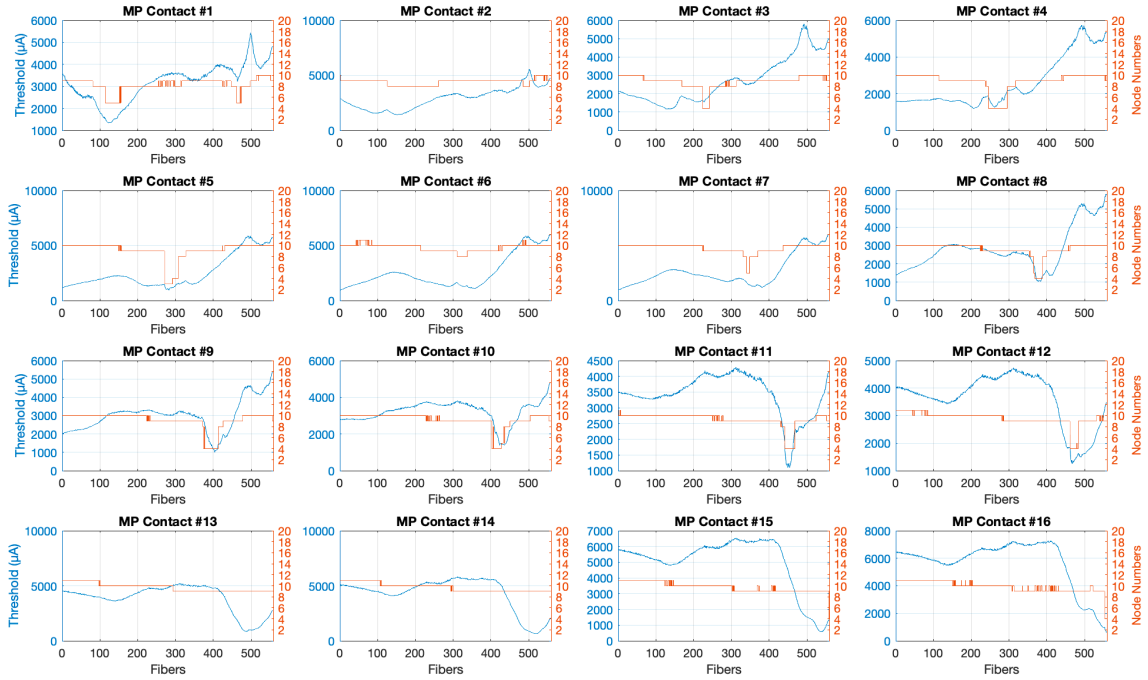

Figure C.1 Threshold Current Profiles for Monopolar Stimulation.

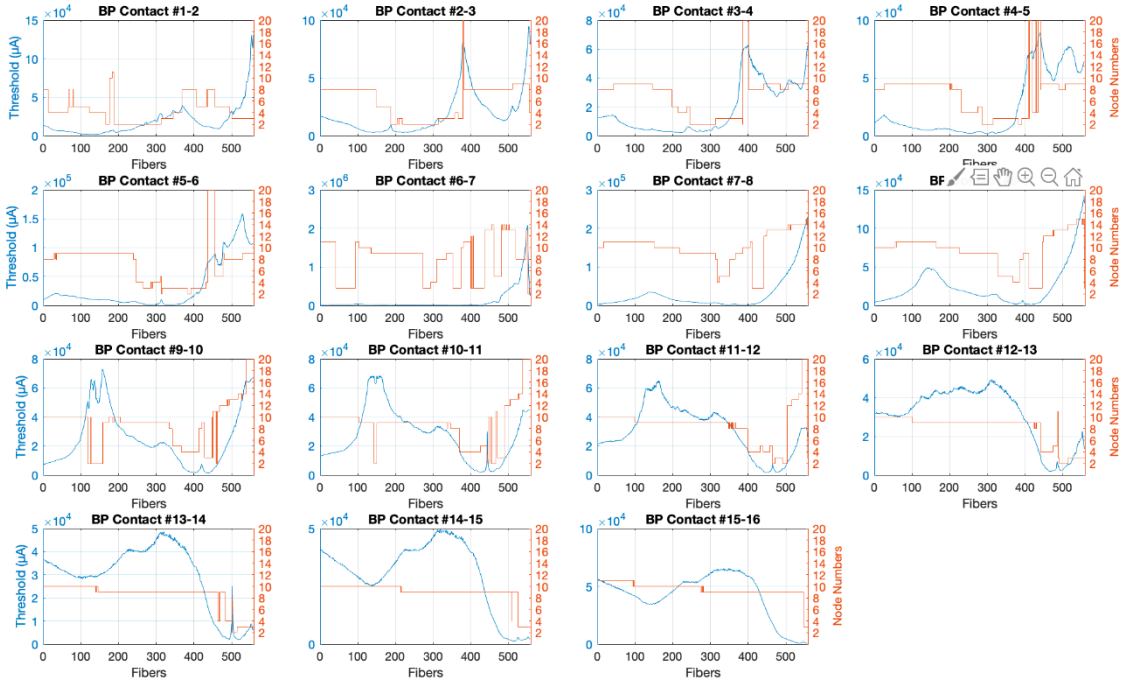

Figure C.2 Threshold Current Profiles for Bipolar Stimulation.

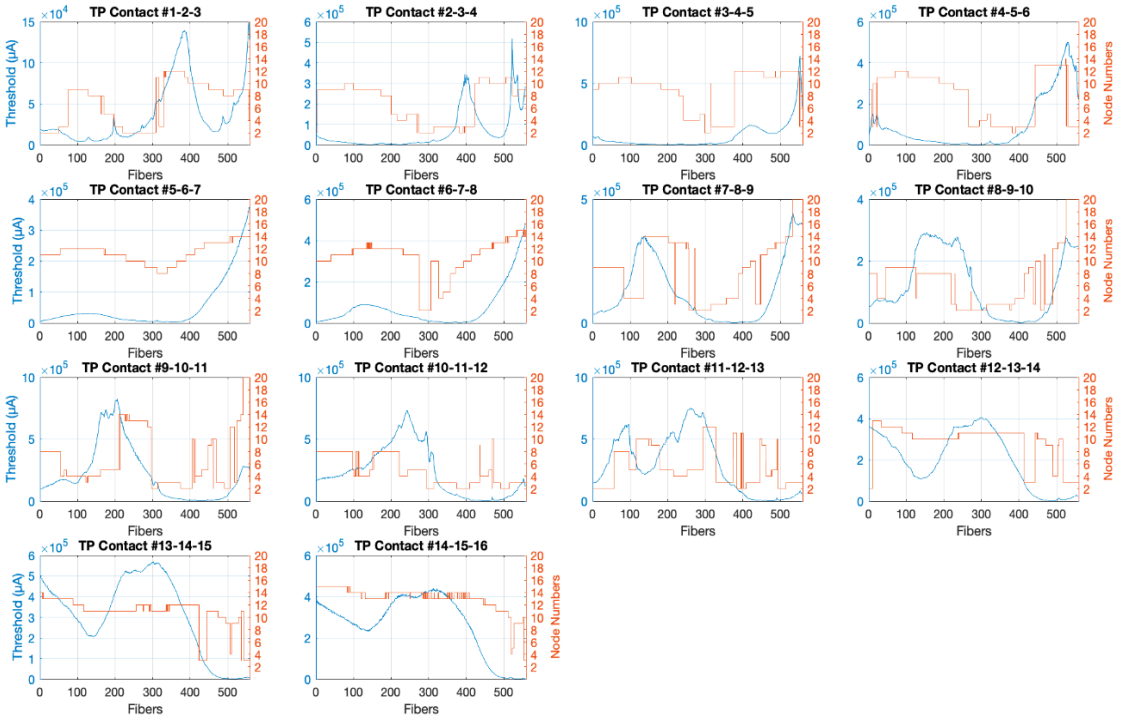

Figure C.3 Threshold Current Profiles for Tripolar Stimulation.

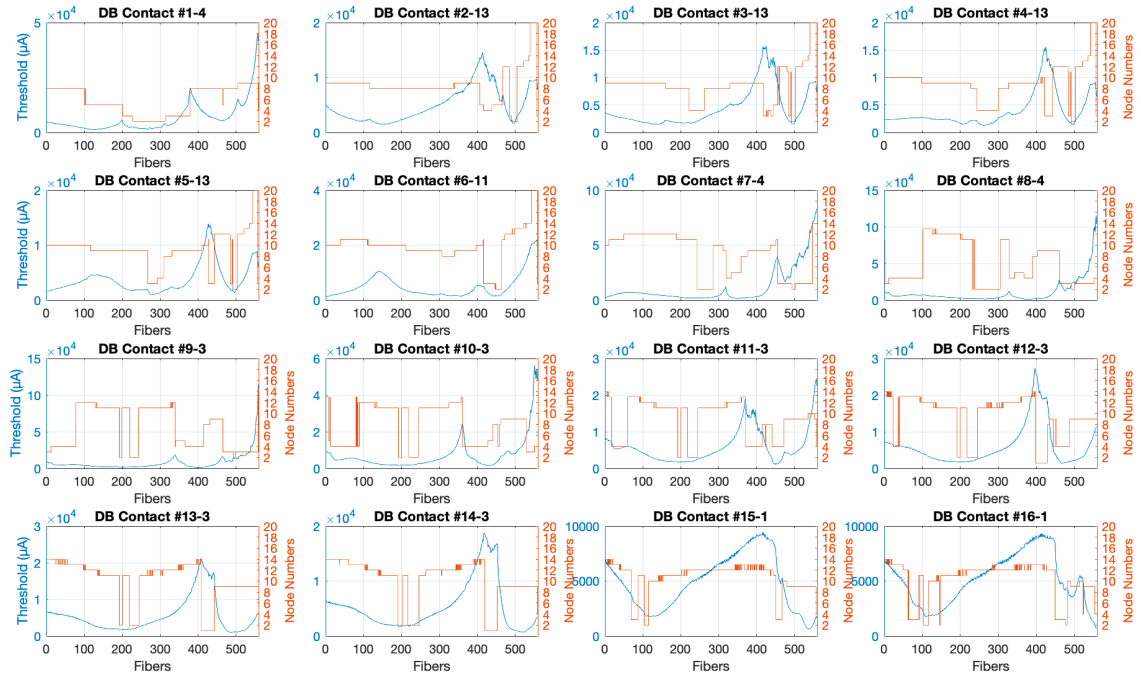

Figure C.4 Threshold Current Profiles for Distant Bipolar Stimulation.

APPENDIX D

NERVE MODEL EQUATIONS

Three consecutive compartmental nodes (k-1, k, k+1) of the GSEF cable model are presented in Figure D.1

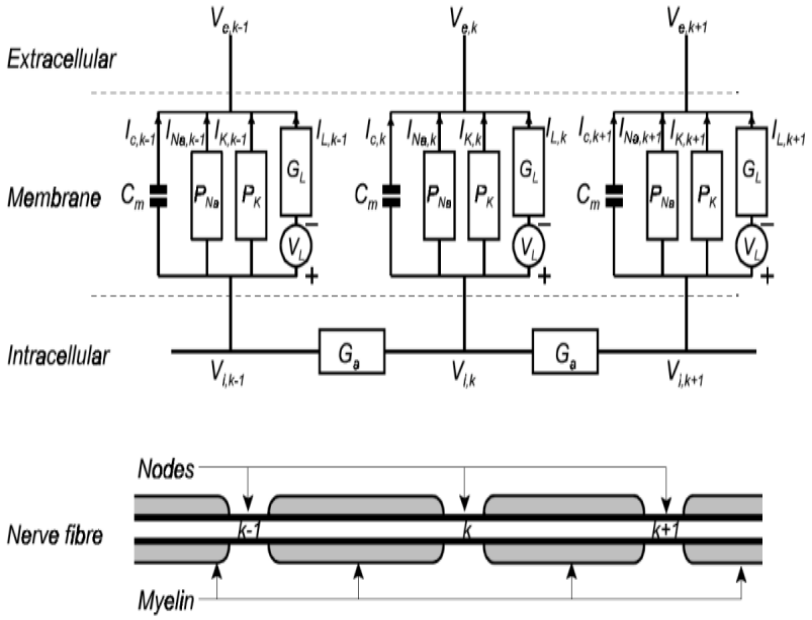

Figure D.1 Three adjacent nodes k-1, k and k+1 is represented in the GSEF model of a myelinated nerve fiber. The upper panel of the figure shows the compartmental circuit model. The lower panel (Nerve fiber) shows the corresponding sections of the axon (myelination with Schwann cells and the nodes of Ranvier) at the same positions of the compartmental model.

Source: Frijns, J. H. M., De Snoo, S. L., & Schoonhoven, R. (1995). Potential distributions and neural excitation patterns in a rotationally symmetric model of the electrically stimulated cochlea. Hearing Research, 87(1-2), 170-186.

The membrane potential is a function of the membrane capacitance C_m, the membrane's permeability to sodium ion P_{Na}, the membrane's permeability to potassium ion P_K, the axoplasmic conductance G_a, the nodal leak conductance G_L, the leak current equilibrium potential V_L, and the external applied electric fields V_e.

Equations below describe the change in membrane potential for node k (Equation D.1).

$$\frac{dV_k}{dt} = \frac{1}{C_m}\left[G_{a,k-1}V_{k-1} - \left(G_{a,k-1} + G_{a,k} + G_{L,k}\right)V_k + G_{a,k}V_{k+1} + G_{a,k-1}V_{e,k-1}\right. \quad \text{(D.1)}$$

$$\left. - \left(G_{a,k-1} + G_{a,k}\right)V_{e,k} + G_{a,k}V_{e,k+1} + I_{act,k} + I_{L,k}\right]$$

where V_k represents the deviation of membrane potential from the resting membrane voltage V_r.

For the first and last nodes:

$$\frac{dV_N}{dt} = \frac{1}{C_m}\left[G_{a,N-1}V_{N-1} - \left(G_{a,N-1} + G_{L,N}\right)V_N + G_{a,N-1}V_{e,N-1} - \left(G_{a,N-1}\right)V_{e,N}\right. \quad \text{(D.2)}$$

$$\left. + I_{act,N} + I_{L,N}\right]$$

The stimulus current I_{act} at a node (Equation D.3):

$$I_{act,k} = I_{Na,k} + I_{K,k} \quad \text{(D.3)}$$

where the active sodium current is (Equation D.4):

$$I_{Na,k} = P_{Na,k}h_k m_k^3 . \frac{E_k F^2}{RT} . \frac{[Na^+]_o - [Na^+]_i \, exp\left(\frac{E_k F}{RT}\right)}{1 - exp\left(\frac{E_k F}{RT}\right)} \quad \text{(D.4)}$$

P_{Na}, m, and h represent the nodal sodium permeability constant, the Na^+ channel activation, and the Na^+ channel inactivation, respectively. $[Na^+]_o$ and $[Na^+]_i$ represent the extracellular and intracellular Na concentrations. T, R and F are the absolute temperature, the gas constant, and Faraday's constant.

The active potassium current I_K is expressed with an equation similar to that of $I_{Na,k}$ (Equation D.5).

$$I_{K,k} = P_{K,k} n_k^2 . \frac{E_k F^2}{RT} . \frac{[K^+]_o - [K^+]_i \, exp\left(\frac{E_k F}{RT}\right)}{1 - exp\left(\frac{E_k F}{RT}\right)} \tag{D.5}$$

where P_K and n represent the nodal potassium permeability constant and the K^+ channel activation. $[K^+]_o$ and $[K^+]_i$ are the extracellular and intracellular K^+ concentrations. The transmembrane potential E_k is the sum of the deviation of the membrane potential V_k and the resting membrane potential V_r (Equation D.6).

$$E_k = V_k + V_r \tag{D.6}$$

The value of V_r is calculated using the Goldman equation (Equation D.7).

$$V_r = \frac{RT}{F} . In\left(\frac{P_k n_o^2 [K^+]_o + P_{Na} h_0 m_0^3 [Na^+]_o}{P_k n_o^2 [K^+]_i + P_{Na} h_0 m_0^3 [Na^+]_i}\right) \tag{D.7}$$

Table D.1. GSEF Model Parameters

Parameters	**Unit**	**Symbol**	**Value**
Length of nodal membrane	cm	l	0.00001
Axonal diameter	cm	d	0.00003
Resistivity of Axoplasm	kΩ-cm	R	0.07
Leak conductance per unit area	$k\Omega^{-1}/cm^2$	g_L	25.78
Nodal potassium permeability	cm/s	P_k	0.000067
Nodal sodium permeability	cm/s	P_{Na}	0.00172
Intracellular potassium concentration	$mmol/cm^3$	$[K^+]_i$	141
Extracellular potassium concentration	$mmol/cm^3$	$[K^+]_o$	4.2
Intracellular sodium concentration	$mmol/cm^3$	$[Na^+]_i$	10
Extracellular sodium concentration	$mmol/cm^3$	$[Na^+]_o$	142
Simulation Temperature	K	T	310.15
Faraday's constant	F	C/mol	96485
Gas Constant	R	mJ/mol/K	8.134

Source: Frijns, J., De Snoo, S., & Schoonhoven, R. (1995). Potential distributions and neural excitation patterns in a rotationally symmetric model of the electrically stimulated cochlea. Hearing Research, 87(1), 170-186.

APPENDIX E

MATLAB SOURCE CODES FOR NEURON MODEL

```
% Initial parameters
%========================================================================
R= 8.314; % Ideal Gas Contant J/Kmol
%T= 301.16; %Absolute Body Temperature K
F = 96485; % Faraday's Constant C/mol

P_K= 2.04e-6; % Potassium Permeability m/s
P_Na= 51.5e-6; % Sodium Permeability  m/s
C_Na_i = 10; %Intracellular Na Concentration mol/m^3
C_Na_o = 142; %Extracellular Na Concentration mol/m^3

C_K_i = 141; %Intracellular K Concentration mol/m^3
C_K_o = 4.2; %Extracellular K Concentration mol/m^3

T0 = 293.15; % Absolute Temperature K
T= 301.16; % Corrected Absolute Temperature K

V0=0; % Inital membrane voltage is zero

% Calculating initial M factor
%========================================================================

% Alpha M for A, B and C
A_alpha_m = 0.49;
B_alpha_m = 25.41;
C_alpha_m = 6.06;

% Beta M for A, B and C
A_beta_m = 1.04;
B_beta_m = 21;
C_beta_m = 9.41;

% Q Factor
Q_10_alpha_M = 2.2;
Q_10_beta_M = 2.2;

x_m_alpha = A_alpha_m * (V0 - B_alpha_m);
y_m_alpha = 1- exp((B_alpha_m-V0)/C_alpha_m);
q_m_alpha = Q_10_alpha_M ^((T-T0)/10);

alpha_m = (x_m_alpha/y_m_alpha) * q_m_alpha;

x_m_beta = A_beta_m * (B_beta_m-V0);
y_m_beta = 1- exp((V0 - B_beta_m)/C_beta_m);
q_m_beta = Q_10_beta_M ^((T-T0)/10);

beta_m = (x_m_beta/y_m_beta) * q_m_beta;

m0 =  alpha_m / (alpha_m + beta_m); % Initial value m = 0.0077
```

```
%Calculating initial N factor
%=====================================================================

% Alpha N for A, B and C
A_alpha_n = 0.02;
B_alpha_n = 35;
C_alpha_n = 10;

% Beta N for A, B and C
A_beta_n = 0.05;
B_beta_n = 10;
C_beta_n = 10;

% Q Factor
Q_10_alpha_N = 3;
Q_10_beta_N = 3;

x_n_alpha = A_alpha_n * (V0 - B_alpha_n);
y_n_alpha = 1- exp((B_alpha_n-V0)/C_alpha_n);
q_n_alpha = Q_10_alpha_N ^((T-T0)/10);

alpha_n = (x_n_alpha/y_n_alpha) * q_n_alpha;

x_n_beta = A_beta_n * (B_beta_n-V0);
y_n_beta = 1- exp((V0 - B_beta_n)/C_beta_n);
q_n_beta = Q_10_beta_N ^((T-T0)/10);

beta_n = (x_n_beta/y_n_beta) * q_n_beta;

n0 =  alpha_n / (alpha_n + beta_n); % Initial value n = 0.0268

%Calculating initial H factor
%=====================================================================

% Alpha H for A, B and C
A_alpha_h = 0.09;
B_alpha_h = -27.74;
C_alpha_h = 9.06;

% Beta H for A, B and C
A_beta_h = 3.7;
B_beta_h = 56;
C_beta_h = 12.5;

% Q Factor
Q_10_alpha_H = 2.9;
Q_10_beta_H = 2.9;

x_h_alpha = A_alpha_h * (B_alpha_h - V0);
y_h_alpha = 1- exp((V0-B_alpha_h)/C_alpha_h);
q_h_alpha = Q_10_alpha_H ^((T-T0)/10);

alpha_h = (x_h_alpha/y_h_alpha) * q_h_alpha;
```

```
x_h_beta = A_beta_h;
y_h_beta = 1 + exp((B_beta_h - V0)/C_beta_h);
q_h_beta = Q_10_beta_H ^((T-T0)/10);
beta_h = (x_h_beta/y_h_beta) * q_h_beta;

h0 =  alpha_h / (alpha_h + beta_h); % Initial value h = 0.7472

%Calculating Resting Potential
%=========================================================================
x = P_K * (n0)^2 * C_K_o;
y = P_Na * (h0)*(m0)^3 * C_Na_o;

a = P_K * (n0)^2 * C_K_i;
b = P_Na * (h0)*(m0)^3 * C_Na_i;

V_rest = 1000 * ((R*T)/F) * log ((x+y)/ (a+b));  % Resting potential
V_rest = -0.0847 (V)

%V_rest = -60;

% 1st NODE PARAMETERS -- PERIPHERAL PROCESS STARTS
%=========================================================================
d_1 = 1.3e-6;  % d_k : axon diameter
l_1 = 10e-6; %  l_k: the nodal gap width --- UNMYELINATED TERMINAL
%*** this is 10 um in Rattay paper, let's use that

L_1 = 250e-6; % The internodal length

% 2nd NODE PARAMETERS
%=========================================================================
d_2 = 1.3e-6;  % d_k : axon diameter
l_2 = 2.5e-6; %  l_k: the nodal gap width
L_2 = 250e-6; % The internodal length

% 3rd NODE PARAMETERS
%=========================================================================
d_3 = 1.3e-6;  % d_k : axon diameter
l_3 = 2.5e-6; %  l_k: the nodal gap width
L_3 = 250e-6; % The internodal length

% 4th NODE PARAMETERS
%=========================================================================
d_4 = 1.3e-6;  % d_k : axon diameter
l_4 = 2.5e-6; %  l_k: the nodal gap width
L_4 = 250e-6; % The internodal length

% 5th NODE PARAMETERS --- PERIPHERAL PROCESS ENDS
%=========================================================================
d_5 = 1.3e-6;  % d_k : axon diameter
l_5 = 2.5e-6; %  l_k: the nodal gap width
L_5 = 210e-6; % The internodal length
```

```
% 6th NODE PARAMETERS --- PRE-SOMATIC
%=========================================================================
d_6 = 1.3e-6;  % d_k : axon diameter
%l_6 = 2.5e-6; %  l_k: the nodal gap width
l_6 = 100e-6; %  l_k: the nodal gap width
L_6 = 100e-6; % The internodal length

% SOMA
%=========================================================================
d_soma = 20e-6;  % d_k : axon diameter
l_soma = 20e-6; %  l_k: the nodal gap width
L_soma = 20e-6; % The internodal length

% 7th NODE PARAMETERS --- POST-SOMATIC
%=========================================================================
%d_7 = 20e-6;  % d_k : axon diameter
d_7 = 2.6e-6;  % d_k : axon diameter
l_7 = 5e-6; %  l_k: the nodal gap width
L_7 = 500e-6; % The internodal length Why not 5e-6
%L_7 = 500e-6; % The internodal length

% 8th NODE PARAMETERS -- CENTRAL PROCESS STARTS
%=========================================================================
d_8 = 2.6e-6;  % d_k : axon diameter
l_8 = 2.5e-6; %  l_k: the nodal gap width
L_8 = 500e-6; % The internodal length

% 9th NODE PARAMETERS
%=========================================================================
d_9 = 2.6e-6;  % d_k : axon diameter
l_9 = 2.5e-6; %  l_k: the nodal gap width
L_9 = 500e-6; % The internodal length

% 10th NODE PARAMETERS
%=========================================================================
d_10 = 2.6e-6;  % d_k : axon diameter
l_10 = 2.5e-6; %  l_k: the nodal gap width
L_10 = 500e-6; % The internodal length

% 11th NODE PARAMETERS
%=========================================================================
d_11 = 2.6e-6;  % d_k : axon diameter
l_11 = 2.5e-6; %  l_k: the nodal gap width
L_11 = 500e-6; % The internodal length

% 12th NODE PARAMETERS
%=========================================================================
d_12 = 2.6e-6;  % d_k : axon diameter
l_12 = 2.5e-6; %  l_k: the nodal gap width
L_12 = 500e-6; % The internodal length

% 13th NODE PARAMETERS
%=========================================================================
d_13 = 2.6e-6;  % d_k : axon diameter
l_13 = 2.5e-6; %  l_k: the nodal gap width
L_13 = 500e-6; % The internodal length
```

```
% 14th NODE PARAMETERS
%=========================================================================
d_14 = 2.6e-6;  % d_k : axon diameter
l_14 = 2.5e-6; %  l_k: the nodal gap width
L_14 = 500e-6; % The internodal length

% 15th NODE PARAMETERS
%=========================================================================
d_15 = 2.6e-6;  % d_k : axon diameter
l_15 = 2.5e-6; %  l_k: the nodal gap width
L_15 = 500e-6; % The internodal length

% 16th NODE PARAMETERS
%=========================================================================
d_16 = 2.6e-6;  % d_k : axon diameter
l_16 = 2.5e-6; %  l_k: the nodal gap width
L_16 = 500e-6; % The internodal length

% 17th NODE PARAMETERS
%=========================================================================
d_17 = 2.6e-6;  % d_k : axon diameter
l_17 = 2.5e-6; %  l_k: the nodal gap width
L_17 = 500e-6; % The internodal length

% 18th NODE PARAMETERS
%=========================================================================
d_18 = 2.6e-6;  % d_k : axon diameter
l_18 = 2.5e-6; %  l_k: the nodal gap width
L_18 = 500e-6; % The internodal length

% 19th NODE PARAMETERS
%=========================================================================
d_19 = 2.6e-6;  % d_k : axon diameter
l_19 = 2.5e-6; %  l_k: the nodal gap width
L_19 = 500e-6; % The internodal length

% G_L (The nodal leak conductance)
%=========================================================================
g_L = 728;   % g_L : the leak conductance per unit area S/m^2

%  Equation: G_L = pi * d_k * l_k * g_L
G_L_1 = pi * d_1 * l_1 * g_L ; % The nodal leak conductance
G_L_2 = pi * d_2 * l_2 * g_L ; % G_L_2
G_L_3 = pi * d_3 * l_3 * g_L ; % G_L_3
G_L_4 = pi * d_4 * l_4 * g_L ; % G_L_4
G_L_5 = pi * d_5 * l_5 * g_L ; % G_L_5
G_L_6 = pi * d_6 * l_6 * g_L ; % G_L_6
G_L_soma = 4 * pi * (d_soma/2)^2 * g_L ; % G_L_soma is a sphere which
has surface area of 4*pi*r^2
G_L_7 = pi * d_7 * l_7 * g_L ; % G_L_7
G_L_8 = pi * d_8 * l_8 * g_L ; % G_L_8
G_L_9 = pi * d_9 * l_9 * g_L ; % G_L_9
G_L_10 = pi * d_10 * l_10 * g_L ; % G_L_10
G_L_11 = pi * d_11 * l_11 * g_L ; % G_L_11
G_L_12 = pi * d_12 * l_12 * g_L ; % G_L_12
G_L_13 = pi * d_13 * l_13 * g_L ; % G_L_13
```

```
G_L_14 = pi * d_14 * l_14 * g_L ; % G_L_14
G_L_15 = pi * d_15 * l_15 * g_L ; % G_L_15
G_L_16 = pi * d_16 * l_16 * g_L ; % G_L_16
G_L_17 = pi * d_17 * l_17 * g_L ; % G_L_17
G_L_18 = pi * d_18 * l_18 * g_L ; % G_L_18
G_L_19 = pi * d_19 * l_19 * g_L ; % G_L_19

% V_L
%=========================================================================
V_L = -84.6;  % The Leak Current Equilibrium Potential

% G_a_k (The axoplasmic conductance)
%=========================================================================
p_i = 0.7; % Axoplasmic Resistivity ohm * m
% Equation: G_a_k = (pi*(d_k^2))/(4*p_i*L_k)

G_a_1 = (pi*(d_1^2))/(4*p_i*L_1); % G_a_1
G_a_2 = (pi*(d_2^2))/(4*p_i*L_2); % G_a_2
G_a_3 = (pi*(d_3^2))/(4*p_i*L_3); % G_a_3
G_a_4 = (pi*(d_4^2))/(4*p_i*L_4); % G_a_4


% Node 5
A =  (pi*(d_5^2))/(4*p_i*L_5);
B =  (pi*(d_6^2))/(4*p_i*L_6 /2); % half of Ga_6--> PRE-SOMA
G_a_5 = 1/(1/A + 1/B) ;  % the formula for adding conductances is G= 1/
(1/G1 + 1/G2)

% PRE-SOMATIC - node 6
A = (pi*(d_6^2))/(4*p_i*L_6 /2); % half of Ga for node 6
B =  (pi*(d_soma^2))/(4*p_i*L_soma /2);  % half of somatic Ga
G_a_6 = 1/(1/A + 1/B); % somatic G_a

% SOMA will be considered as a separate node at the matrix
A = (pi*(d_soma^2))/(4*p_i*L_soma /2); % half of somatic G_a
B = (pi*(d_7^2))/(4*p_i*L_7 /2); % half of Ga_7
G_a_soma =   1/(1/A + 1/B);

% POST-SOMATIC - node 7 - like regular node with a length of (l_7 /2) +
L_7) including the 7th internodal segment
G_a_7 = (pi*(d_7^2))/(4*p_i* (l_7/2 + L_7) );

G_a_8 = (pi*(d_8^2))/(4*p_i*L_8); % G_a_8
G_a_9 = (pi*(d_9^2))/(4*p_i*L_9); % G_a_9
G_a_10 = (pi*(d_10^2))/(4*p_i*L_10); % G_a_10
G_a_11 = (pi*(d_11^2))/(4*p_i*L_11); % G_a_11
G_a_12 = (pi*(d_12^2))/(4*p_i*L_12); % G_a_12
G_a_13 = (pi*(d_13^2))/(4*p_i*L_13); % G_a_13
G_a_14 = (pi*(d_14^2))/(4*p_i*L_14); % G_a_14
G_a_15 = (pi*(d_15^2))/(4*p_i*L_15); % G_a_15
G_a_16 = (pi*(d_16^2))/(4*p_i*L_16); % G_a_16
G_a_17 = (pi*(d_17^2))/(4*p_i*L_17); % G_a_17
G_a_18 = (pi*(d_18^2))/(4*p_i*L_18); % G_a_18
G_a_19 = (pi*(d_19^2))/(4*p_i*L_19); % G_a_19
```

```
% C_m_k (The nodal membrane capacitance)
%=========================================================================
c_m = 0.02; % the membrane capacitance per unit area F/m^2

% Equation: C_m_k = c_m * pi * d_k * l_k;
Cm_1 = c_m * pi * d_1 * l_1; % C_m_1 = 1.8850e-13
Cm_2 = c_m * pi * d_2 * l_2; % C_m_2
Cm_3 = c_m * pi * d_3 * l_3; % C_m_3
Cm_4 = c_m * pi * d_4 * l_4; % C_m_4
Cm_5 = c_m * pi * d_5 * l_5; % C_m_5
Cm_6 = c_m * pi * d_6 * l_6; % C_m_6
Cm_soma = c_m * 4 * pi * (d_soma/2)^2; % C_m_soma is a sphere which has
surface area of 4*pi*r^2
Cm_7 = c_m * pi * d_7 * l_7; % C_m_7
Cm_8 = c_m * pi * d_8 * l_8; % C_m_8
Cm_9 = c_m * pi * d_9 * l_9; % C_m_9
Cm_10 = c_m * pi * d_10 * l_10; % C_m_10
Cm_11 = c_m * pi * d_11 * l_11; % C_m_11
Cm_12 = c_m * pi * d_12 * l_12; % C_m_12
Cm_13 = c_m * pi * d_13 * l_13; % C_m_13
Cm_14 = c_m * pi * d_14 * l_14; % C_m_14
Cm_15 = c_m * pi * d_15 * l_15; % C_m_15
Cm_16 = c_m * pi * d_16 * l_16; % C_m_16
Cm_17 = c_m * pi * d_17 * l_17; % C_m_17
Cm_18 = c_m * pi * d_18 * l_18; % C_m_18
Cm_19 = c_m * pi * d_19 * l_19; % C_m_19

% A, B and C MATRIX FOR GSEF MODEL
% The internodal length, axon diameter, and the nodal gap width are
equal.
%=========================================================================

A_matrix =  [-(G_a_1+G_L_1)/Cm_1 G_a_1/Cm_1 0 0 0 0 0 0 0 0 0 0 0 0 0 0 0
0 0 0 0;
G_a_1/Cm_2 -(G_a_1+G_L_2+G_a_2)/Cm_2 G_a_2/Cm_2 0 0 0 0 0 0 0 0 0 0 0 0 0
0 0 0 0 0;
0 G_a_2/Cm_3 -(G_a_2+G_L_3+G_a_3)/Cm_3 G_a_3/Cm_3 0 0 0 0 0 0 0 0 0 0 0 0
0 0 0 0 0;
0 0 G_a_3/Cm_4 -(G_a_3+G_L_4+G_a_4)/Cm_4 G_a_4/Cm_4 0 0 0 0 0 0 0 0 0 0 0
0 0 0 0 0;
0 0 0 G_a_4/Cm_5 -(G_a_4+G_L_5+G_a_5)/Cm_5 G_a_5/Cm_5 0 0 0 0 0 0 0 0 0 0
0 0 0 0 0;
0 0 0 0 G_a_5/Cm_6 -(G_a_5+G_L_6+G_a_6)/Cm_6 G_a_6/Cm_6 0 0 0 0 0 0 0 0 0
0 0 0 0 0;
0 0 0 0 0 G_a_6/Cm_soma -(G_a_6+G_L_soma+G_a_soma)/Cm_soma
G_a_soma/Cm_soma 0 0 0 0 0 0 0 0 0 0 0 0;  %additional node for soma
0 0 0 0 0 0 G_a_soma/Cm_7 -(G_a_soma+G_L_7+G_a_7)/Cm_7 G_a_7/Cm_7 0 0 0
0 0 0 0 0 0 0 0;
0 0 0 0 0 0 0 G_a_7/Cm_8 -(G_a_7+G_L_8+G_a_8)/Cm_8 G_a_8/Cm_8 0 0 0 0 0
0 0 0 0 0;
0 0 0 0 0 0 0 0 G_a_8/Cm_9 -(G_a_8+G_L_9+G_a_9)/Cm_9 G_a_9/Cm_9 0 0 0 0
0 0 0 0 0;
0 0 0 0 0 0 0 0 0 G_a_9/Cm_10 -(G_a_9+G_L_10+G_a_10)/Cm_10 G_a_10/Cm_10
0 0 0 0 0 0 0 0 0;
0 0 0 0 0 0 0 0 0 0 G_a_10/Cm_11 -(G_a_10+G_L_11+G_a_11)/Cm_11
G_a_11/Cm_11 0 0 0 0 0 0 0;
0 0 0 0 0 0 0 0 0 0 0 G_a_11/Cm_12 -(G_a_11+G_L_12+G_a_12)/Cm_12
G_a_12/Cm_12 0 0 0 0 0 0;
```

```
0 0 0 0 0 0 0 0 0 0 0 0 G_a_12/Cm_13 -(G_a_12+G_L_13+G_a_13)/Cm_13
G_a_13/Cm_13 0 0 0 0 0;
0 0 0 0 0 0 0 0 0 0 0 0 0 G_a_13/Cm_14 -(G_a_13+G_L_14+G_a_14)/Cm_14
G_a_14/Cm_14 0 0 0 0;
0 0 0 0 0 0 0 0 0 0 0 0 0 0 G_a_14/Cm_15 -(G_a_14+G_L_15+G_a_15)/Cm_15
G_a_15/Cm_15 0 0 0;
0 0 0 0 0 0 0 0 0 0 0 0 0 0 0 G_a_15/Cm_16 -
(G_a_15+G_L_16+G_a_16)/Cm_16 G_a_16/Cm_16 0 0;
0 0 0 0 0 0 0 0 0 0 0 0 0 0 0 0 G_a_16/Cm_17 -
(G_a_16+G_L_17+G_a_17)/Cm_17 G_a_17/Cm_17 0;
0 0 0 0 0 0 0 0 0 0 0 0 0 0 0 0 0 G_a_17/Cm_18 -
(G_a_17+G_L_18+G_a_18)/Cm_18 G_a_18/Cm_18;
0 0 0 0 0 0 0 0 0 0 0 0 0 0 0 0 0 0 G_a_18/Cm_19 -
(G_a_18+G_L_19)/Cm_19];

B_matrix = [ -G_a_1/Cm_1 G_a_1/Cm_1 0 0 0 0 0 0 0 0 0 0 0 0 0 0 0 0 0
0;
G_a_1/Cm_2 -(G_a_1+G_a_2)/Cm_2 G_a_2/Cm_2 0 0 0 0 0 0 0 0 0 0 0 0 0 0 0
0 0;
0 G_a_2/Cm_3 -(G_a_2+G_a_3)/Cm_3 G_a_3/Cm_3 0 0 0 0 0 0 0 0 0 0 0 0 0 0
0 0;
0 0 G_a_3/Cm_4 -(G_a_3+G_a_4)/Cm_4 G_a_4/Cm_4 0 0 0 0 0 0 0 0 0 0 0 0 0
0 0;
0 0 0 G_a_4/Cm_5 -(G_a_4+G_a_5)/Cm_5 G_a_5/Cm_5 0 0 0 0 0 0 0 0 0 0 0 0
0 0;
0 0 0 0 G_a_5/Cm_6 -(G_a_5+G_a_6)/Cm_6 G_a_6/Cm_6 0 0 0 0 0 0 0 0 0 0 0
0 0;
0 0 0 0 0 G_a_6/Cm_soma -(G_a_6+G_a_soma)/Cm_soma G_a_soma/Cm_soma 0 0
0 0 0 0 0 0 0 0 0;  % additional node for soma
0 0 0 0 0 0 0 G_a_soma/Cm_7 -(G_a_soma+G_a_7)/Cm_7 G_a_7/Cm_7 0 0 0 0 0 0
0 0 0 0 0;
0 0 0 0 0 0 0 0 G_a_7/Cm_8 -(G_a_7+G_a_8)/Cm_8 G_a_8/Cm_8 0 0 0 0 0 0 0 0
0 0;
0 0 0 0 0 0 0 0 0 G_a_8/Cm_9 -(G_a_8+G_a_9)/Cm_9 G_a_9/Cm_9 0 0 0 0 0 0 0
0 0;
0 0 0 0 0 0 0 0 0 0 G_a_9/Cm_10 -(G_a_9+G_a_10)/Cm_10 G_a_10/Cm_10 0 0 0
0 0 0 0 0;
0 0 0 0 0 0 0 0 0 0 0 G_a_10/Cm_11 -(G_a_10+G_a_11)/Cm_11 G_a_11/Cm_11 0
0 0 0 0 0 0;
0 0 0 0 0 0 0 0 0 0 0 0 G_a_11/Cm_12 -(G_a_11+G_a_12)/Cm_12 G_a_12/Cm_12
0 0 0 0 0 0;
0 0 0 0 0 0 0 0 0 0 0 0 0 G_a_12/Cm_13 -(G_a_12+G_a_13)/Cm_13
G_a_13/Cm_13 0 0 0 0 0;
0 0 0 0 0 0 0 0 0 0 0 0 0 0 G_a_13/Cm_14 -(G_a_13+G_a_14)/Cm_14
G_a_14/Cm_14 0 0 0 0;
0 0 0 0 0 0 0 0 0 0 0 0 0 0 0 G_a_14/Cm_15 -(G_a_14+G_a_15)/Cm_15
G_a_15/Cm_15 0 0 0;
0 0 0 0 0 0 0 0 0 0 0 0 0 0 0 0 G_a_15/Cm_16 -(G_a_15+G_a_16)/Cm_16
G_a_16/Cm_16 0 0;
0 0 0 0 0 0 0 0 0 0 0 0 0 0 0 0 0 G_a_16/Cm_17 -(G_a_16+G_a_17)/Cm_17
G_a_17/Cm_17 0;
0 0 0 0 0 0 0 0 0 0 0 0 0 0 0 0 0 0 G_a_17/Cm_18 -(G_a_17+G_a_18)/Cm_18
G_a_18/Cm_18;
0 0 0 0 0 0 0 0 0 0 0 0 0 0 0 0 0 0 0 G_a_18/Cm_19 -G_a_18/Cm_19];
```

```
C_matrix = [ 1/Cm_1 0 0 0 0 0 0 0 0 0 0 0 0 0 0 0 0 0 0 0;
0 1/Cm_2 0 0 0 0 0 0 0 0 0 0 0 0 0 0 0 0 0 0 0;
0 0 1/Cm_3 0 0 0 0 0 0 0 0 0 0 0 0 0 0 0 0 0 0;
0 0 0 1/Cm_4 0 0 0 0 0 0 0 0 0 0 0 0 0 0 0 0 0;
0 0 0 0 1/Cm_5 0 0 0 0 0 0 0 0 0 0 0 0 0 0 0 0;
0 0 0 0 0 1/Cm_6 0 0 0 0 0 0 0 0 0 0 0 0 0 0 0;
0 0 0 0 0 0 1/Cm_soma 0 0 0 0 0 0 0 0 0 0 0 0 0;  %additional node for
soma
0 0 0 0 0 0 0 1/Cm_7 0 0 0 0 0 0 0 0 0 0 0 0;
0 0 0 0 0 0 0 0 1/Cm_8 0 0 0 0 0 0 0 0 0 0 0;
0 0 0 0 0 0 0 0 0 1/Cm_9 0 0 0 0 0 0 0 0 0 0;
0 0 0 0 0 0 0 0 0 0 1/Cm_10 0 0 0 0 0 0 0 0 0;
0 0 0 0 0 0 0 0 0 0 0 1/Cm_11 0 0 0 0 0 0 0 0;
0 0 0 0 0 0 0 0 0 0 0 0 1/Cm_12 0 0 0 0 0 0 0;
0 0 0 0 0 0 0 0 0 0 0 0 0 1/Cm_13 0 0 0 0 0 0;
0 0 0 0 0 0 0 0 0 0 0 0 0 0 1/Cm_14 0 0 0 0 0;
0 0 0 0 0 0 0 0 0 0 0 0 0 0 0 1/Cm_15 0 0 0 0;
0 0 0 0 0 0 0 0 0 0 0 0 0 0 0 0 1/Cm_16 0 0 0;
0 0 0 0 0 0 0 0 0 0 0 0 0 0 0 0 0 1/Cm_17 0 0;
0 0 0 0 0 0 0 0 0 0 0 0 0 0 0 0 0 0 1/Cm_18 0;
0 0 0 0 0 0 0 0 0 0 0 0 0 0 0 0 0 0 0 1/Cm_19];


d_all = [ d_1 d_2 d_3 d_4 d_5 d_6 d_soma d_7 d_8 d_9 d_10 d_11 d_12
d_13 d_14 d_15 d_16 d_17 d_18 d_19]';
l_all = [ l_1 l_2 l_3 l_4 l_5 l_6 l_soma l_7 l_8 l_9 l_10 l_11 l_12
l_13 l_14 l_15 l_16 l_17 l_18 l_19]';

% Initial time parameters before running neuron model
%=========================================================================
dt = 0.000001; % Temporal resolution or time step [ms]
tmax = 0.002;  % Maximum time of simulation [ms]
t = 0:dt:tmax; % Time vector [ms]
L = length(t); % Number of samples

% Preallocation of V, m, n and h
%=========================================================================
V = zeros(20,L); % for 20 nodes
m = zeros(20,L);  % for 20 nodes
n = zeros(20,L);  % for 20 nodes
h = zeros(20,L);   % for 20 nodes

Na_values = zeros(20,L); % for 20 nodes
K_values = zeros(20,L);  % for 20 nodes
EK_values = zeros(20,L); % for 20 nodes

% Setting initial values of V, m, n and h
%=========================================================================
V(1:20,1) = V0 ;   % for 20 nodes
m(1:20,1) = m0 ;   % for 20 nodes
n(1:20,1) = n0 ;   % for 20 nodes
h(1:20,1) = h0 ;   % for 20 nodes
```

```
%=====================================================================
% Ve: Temporary extracellular potential.
%=====================================================================
Ve=zeros(20,L); % for 20 nodes
PW=0.0001;
%GAP = 0.0002;

Ve(:,1:100)= k * nodes'* ones(1,round ((PW)/dt));

% Euler's method applied to the ordinary differential equations system
for i = 1: L-1

%=====================================================================
    % Calculating E_k TRANSMEMBRANE POTENTIAL
    E_k = (V(1:20,i) + V_rest);
% V_k = E_k - V_r --> E_k = V_k + V_r  Transmembrane potential
    EK_values(1:20,i) = E_k;

%=====================================================================
    % Calculating I_NA SODIUM CURRENT
    I_Na = ( P_Na * h(1:20,i) .* m(1:20,i).^3 .* E_k * (F^2)/(R*T) ) .*
(C_Na_o - C_Na_i * exp( E_k*F/(R*T))) ./ (1-exp( E_k * F/(R * T))) ;
    Na_values(1:20,i) = I_Na;

%=====================================================================
    % Calculating I_K POTASSIUM CURRENT
    I_K = ( P_K * n(1:20,i).^2 .* E_k * (F^2)/(R*T) ) .*  (C_K_o -
C_K_i * exp( E_k*F/(R*T) ) ) ./ (1-exp( E_k * F/(R * T) )) ;
    K_values(1:20,i) = I_K;

%=====================================================================
    % TOTAL SODIUM and POTASSIUM CURRENT
    I_act = I_Na + I_K;

%=====================================================================
    % CALCULATING ACTIVATION POTENTIAL EQUATION

    part_1= A_matrix * V(:,i);
    part_2 = B_matrix * Ve(:,i);
    part_3 = (C_matrix * pi * (d_all(1:20).*l_all(1:20))).* (-(I_act) +
g_L *(V_L -V_rest));
    dV = part_1 + part_2 + part_3;

%=====================================================================
    % CALCULATING V, M, N and H Factors for the next step
    dm = alpha_m .* (1 - m(1:20,i)) - beta_m .* m(1:20,i);
    dn = alpha_n .* (1 - n(1:20,i)) - beta_n .* n(1:20,i);
    dh = alpha_h .* (1 - h(1:20,i)) - beta_h .* h(1:20,i);

    V(1:20,i+1) = V(1:20,i) + dV * dt;
    m(1:20,i+1) = m(1:20,i) + dm * 1000 * dt;
    n(1:20,i+1) = n(1:20,i) + dn * 1000 * dt;
    h(1:20,i+1) = h(1:20,i) + dh * 1000 * dt;
```

```
    % Update of ALPHA_M and BETA_M for the next step

%=========================================================================
    % ALPHA_M
    x_m_Alpha = A_alpha_m * (V(1:20,i+1) - B_alpha_m);
    y_m_Alpha = 1- exp((B_alpha_m-V(1:20,i+1))/C_alpha_m);
    q_m_Alpha = Q_10_alpha_M ^((T-T0)/10);
    alpha_m = (x_m_Alpha./y_m_Alpha) * q_m_Alpha; %ALPHA M

%=========================================================================
    % BETA_M
    x_m_Beta = A_beta_m * (B_beta_m-V(1:20,i+1));
    y_m_Beta = 1- exp((V(1:20,i+1) - B_beta_m)/C_beta_m);
    q_m_Beta = Q_10_beta_M ^((T-T0)/10);
    beta_m = (x_m_Beta ./ y_m_Beta) * q_m_Beta; %BETA M

    % Update of ALPHA_H and BETA_H for the next step

%=========================================================================
    % ALPHA_H
    x_h_Alpha = A_alpha_h * (B_alpha_h - V(1:20,i+1));
    y_h_Alpha = 1- exp((V(1:20,i+1)-B_alpha_h)/C_alpha_h);
    q_h_Alpha = Q_10_alpha_H ^((T-T0)/10);
    alpha_h = (x_h_Alpha ./ y_h_Alpha) * q_h_Alpha; %ALPHA H

%=========================================================================
    % BETA_H
    x_h_Beta = A_beta_h;
    y_h_Beta = 1 + exp((B_beta_h - V(1:20,i+1))/C_beta_h);
    q_h_Beta = Q_10_beta_H ^((T-T0)/10);
    beta_h = (x_h_Beta ./ y_h_Beta) * q_h_Beta; %%BETA H

    % Update of ALPHA_N and BETA_N for the next step

%=========================================================================
    % ALPHA_N
    x_n_Alpha = A_alpha_n * (V(1:20,i+1) - B_alpha_n);
    y_n_Alpha = 1- exp((B_alpha_n-V(1:20,i+1))/C_alpha_n);
    q_n_Alpha = Q_10_alpha_N ^((T-T0)/10);
    alpha_n = (x_n_Alpha ./ y_n_Alpha) * q_n_Alpha; %ALPHA N

%=========================================================================
    % BETA_N
    x_n_Beta = A_beta_n * (B_beta_n-V(1:20,i+1));
    y_n_Beta = 1- exp((V(1:20,i+1) - B_beta_n)/C_beta_n);
    q_n_Beta = Q_10_beta_N ^((T-T0)/10);
    beta_n = (x_n_Beta ./ y_n_Beta) * q_n_Beta; %BETA N


end
end
```

REFERENCES

Badenhorst, W., Hanekom, T., & Hanekom, J. J. (2016). Development of a voltage-dependent current noise algorithm for conductance-based stochastic modelling of auditory nerve fibres. *Biological Cybernetics, 110*(6), 403-416.

Bai, S., Encke, J., Obando-Leitón, M., Weiß, R., Schäfer, F., Eberharter, J., . . . Hemmert, W. (2019). Electrical stimulation in the human cochlea: a computational study based on high-resolution micro-CT scans. *Frontiers in Neuroscience, 13*, 1312.

Bonham, B. H., & Litvak, L. M. (2008). Current focusing and steering: modeling, physiology, and psychophysics. *Hearing Research, 242*(1-2), 141-153.

Braun, K., Böhnke, F., & Stark, T. (2012). Three-dimensional representation of the human cochlea using micro-computed tomography data: presenting an anatomical model for further numerical calculations. *Acta oto-laryngologica, 132*(6), 603-613.

Briaire, J. J., & Frijns, J. H. (2006). The consequences of neural degeneration regarding optimal cochlear implant position in scala tympani: a model approach. *Hearing Research, 214*(1-2), 17-27.

Cakir, A., Labadie, R. F., & Noble, J. H. (2019). *Auditory nerve fiber segmentation methods for neural activation modeling.* Paper presented at the Medical Imaging 2019: Image-Guided Procedures, Robotic Interventions, and Modeling.

Carlyon, R. P., & Goehring, T. (2021). Cochlear implant research and development in the twenty-first century: a critical update. *Journal of the Association for Research in Otolaryngology, 22*(5), 481-508.

Cheng, Q., Yu, H., Liu, J., Zheng, Q., Bai, Y., & Ni, G. (2022). Design and optimization of auditory prostheses using the finite element method: a narrative review. *Annals of Translational Medicine, 10*(12).

Choi, C., & Hsu, C.-H. (2009). Conditions for generating virtual channels in cochlear prosthesis systems. *Annals of Biomedical Engineering, 37*(3), 614-624.

Cosentino, S., Deeks, J. M., & Carlyon, R. P. (2015). Procedural factors that affect psychophysical measures of spatial selectivity in cochlear implant users. *Trends in Hearing, 19*, 2331216515607067.

Dang, K., Clerc, M., Vandersteen, C., Guevara, N., & Gnansia, D. (2015). *In situ validation of a parametric model of electrical field distribution in an implanted cochlea.* Paper presented at the 2015 7th International IEEE/EMBS Conference on Neural Engineering (NER).

Dhanasingh, A., & Jolly, C. (2017). An overview of cochlear implant electrode array designs. *Hearing Research, 356*, 93-103.

Erixon, E., & Rask-Andersen, H. (2013). How to predict cochlear length before cochlear implantation surgery. *Acta oto-laryngologica, 133*(12), 1258-1265.

Escudé, B., James, C., Deguine, O., Cochard, N., Eter, E., & Fraysse, B. (2006). The size of the cochlea and predictions of insertion depth angles for cochlear implant electrodes. *Audiology and Neurotology, 11*(Suppl. 1), 27-33.

Fellner, A., Heshmat, A., Werginz, P., & Rattay, F. (2022). A finite element method framework to model extracellular neural stimulation. *Journal of Neural Engineering, 19*(2), 022001.

Frankenhaeuser, B., & Huxley, A. (1964). The action potential in the myelinated nerve fibre of Xenopus laevis as computed on the basis of voltage clamp data. *The Journal of Physiology, 171*(2), 302-315.

Frijns, J., De Snoo, S., & Schoonhoven, R. (1995a). Potential distributions and neural excitation patterns in a rotationally symmetric model of the electrically stimulated cochlea. *Hearing Research, 87*(1), 170-186.

Frijns, J., De Snoo, S., & Schoonhoven, R. (1995b). Potential distributions and neural excitation patterns in a rotationally symmetric model of the electrically stimulated cochlea. *Hearing Research, 87*(1-2), 170-186.

Frijns, J., De Snoo, S., & Ten Kate, J. (1996). Spatial selectivity in a rotationally symmetric model of the electrically stimulated cochlea. *Hearing Research, 95*(1-2), 33-48.

Frijns, J., Van Gendt, M., Kalkman, R., & Briaire, J. (2015). *Modeled neural response patterns from various speech coding strategies.* Paper presented at the Conference on Implantable Auditory Prostheses.

Frijns, J. H., Briaire, J. J., & Grote, J. J. (2001). The importance of human cochlear anatomy for the results of modiolus-hugging multichannel cochlear implants. *Otology and Neurotology, 22*(3), 340-349.

Frijns, J. H., Briaire, J. J., & Schoonhoven, R. (2000). Integrated use of volume conduction and neural models to simulate the response to cochlear implants. *Simulation Practice and Theory, 8*(1), 75-97.

Frijns, J. H., Dekker, D. M., & Briaire, J. J. (2011). Neural excitation patterns induced by phased-array stimulation in the implanted human cochlea. *Acta oto-laryngologica, 131*(4), 362-370.

Frijns, J. H., Kalkman, R. K., Vanpoucke, F. J., Bongers, J. S., & Briaire, J. J. (2009). Simultaneous and non-simultaneous dual electrode stimulation in cochlear implants: evidence for two neural response modalities. *Acta oto-laryngologica, 129*(4), 433-439.

Frijns, J. H., Mooij, J., & Ten Kate, J. (1994). A quantitative approach to modeling mammalian myelinated nerve fibers for electrical prosthesis design. *IEEE Transactions on Biomedical Engineering, 41*(6), 556-566.

Frijns, J. H. M. (1995). *Cochlear implants: a modelling approach*. *Ph.D. Thesis, Leiden University, Leiden, The Netherlands.*

Gerber, N., Reyes, M., Barazzetti, L., Kjer, H. M., Vera, S., Stauber, M., . . . Wimmer, W. (2017a). A multiscale imaging and modelling dataset of the human inner ear. *Scientific Data, 4*, 170132.

Gerber, N., Reyes, M., Barazzetti, L., Kjer, H. M., Vera, S., Stauber, M., . . . Wimmer, W. (2017b). A multiscale imaging and modelling dataset of the human inner ear. *Scientific Data, 4*(1), 1-12.

Goldwyn, J. H., Bierer, S. M., & Bierer, J. A. (2010). Modeling the electrode–neuron interface of cochlear implants: Effects of neural survival, electrode placement, and the partial tripolar configuration. *Hearing Research, 268*(1-2), 93-104.

Gorman, P. H., & Mortimer, J. T. (1983). The effect of stimulus parameters on the recruitment characteristics of direct nerve stimulation. *IEEE Transactions on Biomedical Engineering*(7), 407-414.

Hanekom, T. (2001). Three-dimensional spiraling finite element model of the electrically stimulated cochlea. *Ear and Hearing, 22*(4), 300-315.

Hanekom, T. (2005). Modelling encapsulation tissue around cochlear implant electrodes. *Medical and Biological Engineering and Computing, 43*(1), 47-55.

Hanekom, T., & Hanekom, J. J. (2016). Three-dimensional models of cochlear implants: a review of their development and how they could support management and maintenance of cochlear implant performance. *Network: Computation in Neural Systems, 27*(2-3), 67-106.

Heshmat, A., Sajedi, S., Schrott-Fischer, A., & Rattay, F. (2021). Polarity Sensitivity of Human Auditory Nerve Fibers Based on Pulse Shape, Cochlear Implant Stimulation Strategy and Array. *Frontiers in Neuroscience, 15*.

Kalkman, R. K., Briaire, J. J., Dekker, D. M., & Frijns, J. H. (2014). Place pitch versus electrode location in a realistic computational model of the implanted human cochlea. *Hearing Research, 315*, 10-24.

Kalkman, R. K., Briaire, J. J., & Frijns, J. H. (2015). Current focussing in cochlear implants: an analysis of neural recruitment in a computational model. *Hearing Research, 322*, 89-98.

Kalkman, R. K., Briaire, J. J., & Frijns, J. H. (2016). Stimulation strategies and electrode design in computational models of the electrically stimulated cochlea: An overview of existing literature. *Network: Computation in Neural Systems, 27*(2-3), 107-134.

Kikidis, D., & Bibas, A. (2014). A clinically oriented introduction and review on finite element models of the human cochlea. *BioMed Research International, 2014*.

Koch, D. B., Downing, M., Osberger, M. J., & Litvak, L. (2007). Using current steering to increase spectral resolution in CII and HiRes 90K users. *Ear and Hearing, 28*(2), 38S-41S.

Lenarz, T. (2017). Cochlear implant–state of the art. *Laryngo-rhino-otologie, 96*(S 01), S123-S151.

Litvak, L. M., Spahr, A. J., & Emadi, G. (2007). Loudness growth observed under partially tripolar stimulation: model and data from cochlear implant listeners. *The Journal of the Acoustical Society of America, 122*(2), 967-981.

Luo, X., Wu, C.-C., & Pulling, K. (2021). Combining current focusing and steering in a cochlear implant processing strategy. *International Journal of Audiology, 60*(3), 232-237.

Mangado, N., Ceresa, M., Benav, H., Mistrik, P., Piella, G., & Ballester, M. A. G. (2018). Towards a complete in silico assessment of the outcome of cochlear implantation surgery. *Molecular Neurobiology, 55*(1), 173-186.

Potrusil, T., Heshmat, A., Sajedi, S., Wenger, C., Chacko, L. J., Glueckert, R., . . . Rattay, F. (2020). Finite element analysis and three-dimensional reconstruction of tonotopically aligned human auditory fiber pathways: a computational environment for modeling electrical stimulation by a cochlear implant based on micro-CT. *Hearing Research, 393*, 108001.

Ranck Jr, J. B. (1975). Which elements are excited in electrical stimulation of mammalian central nervous system: a review. *Brain Research, 98*(3), 417-440.

Rattay, F. (1986). Analysis of models for external stimulation of axons. *IEEE Transactions on Biomedical Engineering*(10), 974-977.

Rattay, F. (1987). Ways to approximate current-distance relations for electrically stimulated fibers. *Journal of Theoretical Biology, 125*(3), 339-349.

Rattay, F. (1989). Analysis of models for extracellular fiber stimulation. *IEEE Transactions on Biomedical Engineering, 36*(7), 676-682.

Rattay, F. (1999). The basic mechanism for the electrical stimulation of the nervous system. *Neuroscience, 89*(2), 335-346.

Rattay, F. (2008). Current distance relations for fiber stimulation with pointsources. *IEEE Transactions on Biomedical Engineering, 55*(3), 1122-1127.

Rattay, F., Bassereh, H., & Fellner, A. (2017). Impact of electrode position on the elicitation of sodium spikes in retinal bipolar cells. *Scientific Reports, 7*(1), 1-12.

Rattay, F., Leao, R. N., & Felix, H. (2001). A model of the electrically excited human cochlear neuron. II. Influence of the three-dimensional cochlear structure on neural excitability. *Hearing Research, 153*(1-2), 64-79.

Rattay, F., & Tanzer, T. (2022). Impact of electrode position on the dynamic range of a human auditory nerve fiber. *Journal of Neural Engineering, 19*(1), 016025.

Rubinstein, J. (1993). Axon termination conditions for electrical stimulation. *IEEE Transactions on Biomedical Engineering, 40*(7), 654-663.

Seeber, B. U., & Bruce, I. C. (2016). The history and future of neural modeling for cochlear implants. *Network: Computation in Neural Systems, 27(2-3), 53-66.*

Smit, J., Hanekom, T., & Hanekom, J. J. (2008). Predicting action potential characteristics of human auditory nerve fibres through modification of the Hodgkin-Huxley equations. *South African Journal of Science, 104*(7), 284-292.

Snel-Bongers, J., Briaire, J. J., van der Veen, E. H., Kalkman, R. K., & Frijns, J. H. (2013). Threshold levels of dual electrode stimulation in cochlear implants. *Journal of the Association for Research in Otolaryngology, 14*(5), 781-790.

Teymouri, J., Hullar, T. E., Holden, T. A., & Chole, R. A. (2011). Verification of computed tomographic estimates of cochlear implant array position: A micro-CT and histological analysis. *Otology and Neurotology: Official Publication of the American Otological Society, American Neurotology Society [and] European Academy of Otology and Neurotology, 32*(6), 980.

Warman, E. N., Grill, W. M., & Durand, D. (1992). Modeling the effects of electric fields on nerve fibers: determination of excitation thresholds. *IEEE Transactions on Biomedical Engineering, 39*(12), 1244-1254.

Wilson, B. S., Finley, C. C., Lawson, D. T., Wolford, R. D., Eddington, D. K., & Rabinowitz, W. M. (1991). Better speech recognition with cochlear implants. *Nature, 352*(6332), 236-238.

Yushkevich, P. A., Piven, J., Hazlett, H. C., Smith, R. G., Ho, S., Gee, J. C., & Gerig, G. (2006). User-guided 3D active contour segmentation of anatomical structures: significantly improved efficiency and reliability. *Neuroimage, 31*(3), 1116-1128.

Zeng, F.-G. (2017). Challenges in improving cochlear implant performance and accessibility. *IEEE Transactions on Biomedical Engineering, 64*(8), 1662-1664.

Zhu, Z., Tang, Q., Zeng, F.-G., Guan, T., & Ye, D. (2012). Cochlear-implant spatial selectivity with monopolar, bipolar and tripolar stimulation. *Hearing Research, 283*(1-2), 45-58.